ACS NANO

www.acsnano.org

ARTICLE

Patterns of Flexible Nanotubes Formed by Liquid-Ordered and Liquid-Disordered Membranes

Yonggang Liu,[†,‡] Jaime Agudo-Canalejo,[†] Andrea Grafmüller,[†] Rumiana Dimova,[†] and Reinhard Lipowsky*[,†]

[†]Theory & Biosystems, Max Planck Institute of Colloids and Interfaces, 14424 Potsdam, Germany

[‡]State Key Laboratory of Polymer Physics and Chemistry, Changchun Institute of Applied Chemistry, Chinese Academy of Sciences, 130022 Changchun, China

Supporting Information

ABSTRACT: **Biological membranes form both intra- and intercellular nanotubes that are used for molecular sorting within single cells and for long-distance connections between different cells. Such nanotubes can also develop from synthetic lipid bilayers in their fluid state. Each nanotube has a large area-to-volume ratio and stably encloses a water channel that is thereby shielded from its surroundings. The tubes are rather flexible and can easily change both their length and their conformation. Here, we study nanotubes formed by liquid-ordered (Lo) and liquid-disordered (Ld) membranes with three lipid components exposed to aqueous mixtures of two polymers, polyethylene glycol (PEG) and dextran. Both types of membranes form striking patterns of nanotubes when we reduce the volume of giant vesicles by osmotic deflation, thereby exposing the two bilayer leaflets of the membranes to polymer solutions of different composition. With decreasing volume, three different patterns are observed corresponding to three distinct vesicle morphologies that reflect the interplay of spontaneous curvature and aqueous phase separation. We show that tube nucleation and growth is governed by two kinetic pathways and that the tubes undergo a novel shape transformation from necklace-like to cylindrical tubes at a certain critical tube length. We deduce the spontaneous curvature generated by the membrane-polymer interactions from the observed vesicle morphologies using three different and independent methods of image analysis. The spontaneous curvature of the Ld membranes is found to be 4.7 times larger than that of the Lo membranes. We also show that these curvatures are generated by weak PEG adsorption onto the membranes, with a binding affinity of about 1.6 k_BT per chain. In this way, our study provides a direct connection between nanoscopic membrane shapes and molecular interactions. Our approach is rather general and can be applied to many other systems of interest such as polymersomes or membrane-bound proteins and peptides.**

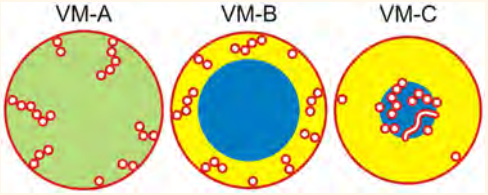

KEYWORDS: *membranes and vesicles, aqueous polymer solutions, membrane nanotubes, tube nucleation and growth, bilayer asymmetry, spontaneous curvature, PEG adsorption*

One important function of biological membranes is to partition space into separate compartments. Particularly interesting compartments are provided by membrane nanotubes which represent highly curved membrane structures, have a large area-to-volume ratio, thereby enhancing membrane-dependent processes, and stably enclose thin water channels which are well-separated and shielded from their surroundings. Intracellular nanotubes are ubiquitous structural elements of many membrane-bound organelles such as the endoplasmic reticulum, the Golgi, the endosomal network, and mitochondria.[1−3] These nanotubes connect distant parts of the cell and are used for molecular sorting, signaling, and transport. Intercellular (or "tunneling") nanotubes between two or more cells provide long-distance connections for cell−cell communication, intercellular transport, and virus infections.[4−6] Synthetic nanotubes formed by lipid or polymer bilayers have been studied in the context of bilayer asymmetry and spontaneous curvature,[7,8] lipid and protein sorting,[9,10] cellular delivery of drugs and other chemical agents,[11] and as templates for rigid "nanowires".[12]

Biological and biomimetic nanotubes are formed by fluid membranes which have a stable bilayer structure on the molecular scale but are highly flexible on the nanoscopic scale. The fluidity also allows fast lateral transport of molecules along the membranes, easy changes in tube length and conformation, as well as the formation of intramembrane domains and rafts.

Received: August 27, 2015
Accepted: November 20, 2015
Published: November 20, 2015

DOI: 10.1021/acsnano.5b05377
ACS Nano 2016, 10, 463−474

Here, we study giant unilamellar vesicles of three-component lipid bilayers. We investigate and compare two different lipid compositions that form a liquid-ordered (Lo) and a liquid-disordered (Ld) phase. The vesicles enclose aqueous polymer mixtures of dextran and polyethylene glycol (PEG), an aqueous two-phase system that has been frequently used in biochemical analysis and biotechnology[13] to separate and purify biomolecules, cell organelles, and cell membranes. The lipid membranes form striking patterns of nanotubes within the giant vesicles when we deflate these vesicles osmotically, thereby exposing the two bilayer leaflets to polymer solutions of different composition. Three types of nanotube patterns can be distinguished corresponding to three different vesicle morphologies as shown schematically in Figure 1.

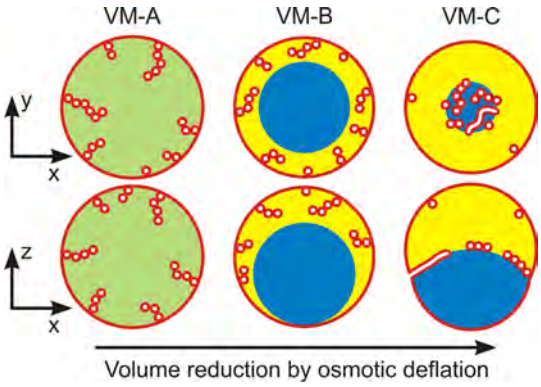

Figure 1. Three nanotube patterns corresponding to the distinct vesicle morphologies VM-A, VM-B, and VM-C observed along the deflation path: Schematic views of horizontal *xy*-scans (top row) and of vertical *xz*-scans (bottom row) across the deflated vesicles. In all cases, the tubes are filled with external medium (white). For the VM-A morphology, the interior polymer solution is uniform (green), whereas it is phase separated (blue-yellow) for the morphologies VM-B and VM-C, with complete and partial wetting, respectively, of the membrane by the PEG-rich aqueous phase (yellow). For the VM-B morphology, the nanotubes explore the whole PEG-rich (yellow) droplet but stay away from the dextran-rich (blue) one. For the VM-C morphology, the nanotubes adhere to the interface between the two aqueous droplets forming a thin and crowded layer along this interface. The different nanotube patterns can be most easily visualized by three-dimensional confocal scans of the vesicles, see Supporting Movies.

The theoretical analysis of these observations reveals that the tubes are nucleated from small buds which subsequently grow into necklace-like tubes. The necklaces are further extended until they transform into cylindrical tubes when their length exceeds a certain critical value. The critical length can be reduced by the adhesion of the nanotubes to interfaces. These morphological features are universal and apply to the deflation-induced formation of membrane nanotubes in general.

The magnitude of the bilayer asymmetry, arising from the exposure of the two leaflets to different polymer concentrations, is quantitatively described by the spontaneous curvature of the membranes. We introduce three different and independent methods of image analysis to deduce this curvature from the observed vesicle morphologies. All three methods give very consistent results. The spontaneous curvature m of the Ld and Lo membranes is found to be $m_{Ld} \simeq -1/(125\ \text{nm})$ and $m_{Lo} \simeq -1/(600\ \text{nm})$ over a certain range of polymer concentrations. Using atomistic molecular dynamics simulations, we also elucidate the molecular mechanism for the spontaneous curvatures obtained here and conclude that these curvatures are generated by the weak adsorption of PEG chains onto the membranes, with a binding free energy of about 4 kJ/mol or 1.6 k_BT per chain, and that the curvature ratio $m_{Ld}/m_{Lo} \simeq 4.7$ is approximately equal to the ratio κ_{Lo}/κ_{Ld} of the corresponding bending rigidities. Our approach to deduce the spontaneous curvature from the observed tubulation process is quite general and can be extended to other membrane systems of interest. Two examples are provided by polymer bilayers or polymersomes[11,14−16] and by the adsorption of proteins[17,18] or peptides[19] onto lipid membranes. Accurate estimates for the spontaneous curvature are also crucial in order to determine the critical particle sizes for the engulfment of nanoparticles by membranes and vesicles.[20]

RESULTS AND DISCUSSION

Tubulation of Vesicles Induced by Osmotic Deflation.

Giant unilamellar vesicles were prepared from ternary lipid mixtures of dioleoylphosphatidylcholine (DOPC), dipalmitoylphosphatidylcholine (DPPC), and cholesterol, see Methods. The vesicles were formed in aqueous polymer mixtures of PEG and dextran, which undergo phase separation into two aqueous phases, a PEG-rich and a dextran-rich phase, when the polymer weight fractions exceed a few weight percent[13,21,22] (Figure 2a,b). Two types of lipid compositions were studied corresponding to a flexible Ld and a more rigid Lo membrane.[23−25] The Ld membranes were fluorescently labeled by a red dye, the Lo membranes by a green one (Figure 2c,d and Supporting Information Movies).

Our experiments started with spherical vesicles that enclosed a homogeneous polymer solution (composition 0 in Figure 2b). These vesicles were then deflated osmotically by using exterior solutions that contained fixed weight fractions of the two polymers but an increasing amount of sucrose. The subsequent deflation steps are depicted in Figure 2b and described in more detail in Table S1. After the first deflation step, the interior polymer solution still formed a uniform aqueous phase (composition 1), corresponding to the VM-A morphology in Figure 1. After the second and all subsequent deflation steps, the interior solution underwent phase separation into a PEG-rich and a dextran-rich phase which formed two aqueous droplets within the vesicles. The shapes of these droplets could be directly imaged by differential interference contrast and fluorescence microscopy, see Figure S1. The PEG-rich droplet was always in contact with the membranes, whereas the dextran-rich droplet came into contact with the Ld and Lo membranes only after the third and fourth deflation step, respectively. Therefore, the Ld membranes were completely wetted by the PEG-rich phase for composition 2, while the Lo membranes exhibited the same type of wetting for compositions 2 and 3, corresponding to the VM-B morphology in Figure 1. Subsequent deflation steps led to the VM-C morphology with partial membrane wetting and nonzero contact angles.

Each osmotic deflation step reduces the vesicle volume and, thus, increases the area-to-volume ratio of the vesicle. In the absence of polymers, vesicles undergo smooth shape transformations from spherical toward prolate shapes as studied previously[26,27] for one-component membranes. In contrast to such conventional shape transformations, the vesicles studied here still assumed a spherical shape after the initial deflation steps, both for the flexible Ld membranes (Figure 2c) and for

DOI: 10.1021/acsnano.5b05377
ACS Nano 2016, 10, 463−474

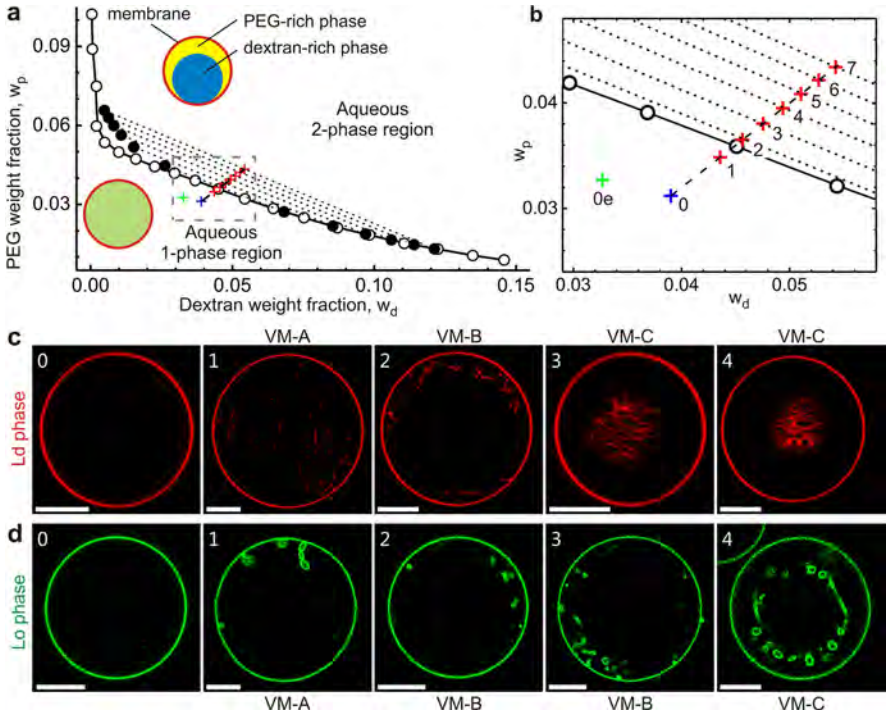

Figure 2. Osmotic deflation and tubulation of vesicles in aqueous PEG−dextran solutions. (a) High-precision phase diagram of aqueous PEG−dextran solution close to its critical demixing point at 24 °C with dotted tie lines and dashed deflation trajectory. (b) Enlarged region of phase diagram around the deflation trajectory which starts from the initial polymer composition 0 (blue cross) within the vesicle and the composition 0e (green cross) of the isotonic external medium. The vesicle is then osmotically deflated in a stepwise manner which leads to the interior compositions 1−7 (red crosses), see Table S1 for more details. (c) Confocal *xy*-scans of vesicles bounded by an Ld membrane (red) at the deflation steps 0−4. Apart from the initial vesicle 0, all deflated vesicles formed membrane nanotubes pointing into the vesicle interior. The thickness of the Ld tubes was below optical resolution. More detailed views of the three-dimensional morphologies of the vesicles are provided in the Movies Ld_1, Ld_2, and Ld_4. (d) Confocal *xy*-scans of vesicles bounded by an Lo membrane (green) at the deflation points 0−4. The deflated vesicles in panels 1−4 again form nanotubes; the corresponding three-dimensional scans are shown in the Movies Lo_1, Lo_2, and Lo_4. The thickness of the Lo tubes was above optical resolution. The scale bars are 10 μm in all confocal images. The confocal *xz*-scans of the vesicles in panels (c) and (d) are displayed in Figure S2.

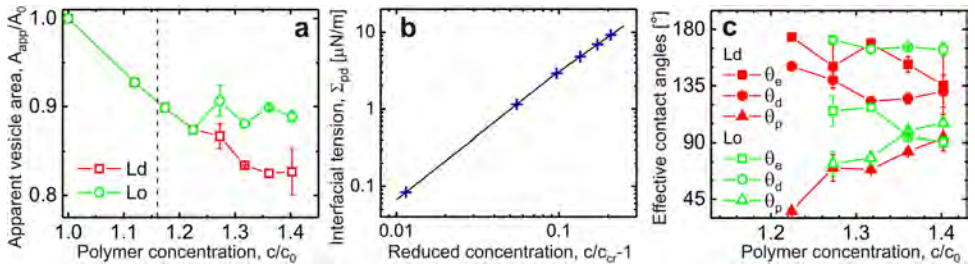

Figure 3. Variation of apparent vesicle area, interfacial tension, and contact angles with osmotic deflation which leads to an increase in the total polymer concentration c within the vesicles. (a) Apparent membrane area of large mother vesicles which decreases monotically during the first three deflation steps both for the Ld and the Lo membranes. The concentration c_0 = 0.0714 g/cm^3 represents the initial polymer concentration before deflation; the vertical dashed line corresponds to the critical concentration c_{cr} = 1.161 c_0. (b) Interfacial tension Σ_{pd} of the pd interface (p, PEG-rich phase; d, dextran-rich phase) between the PEG-rich and dextran-rich aqueous phases, data (blue crosses) and linear fit (solid black line). The tension vanishes at the critical concentration and increases monotonically for $c > c_{cr}$. (c) Effective contact angles θ_p, θ_d, and θ_e between the pd interface and the two membrane segments as defined in Figure S3. The contact angle θ_p vanishes at the concentration c_{wt} of the complete-to-partial wetting transition with 1.174 < c_{wt}/c_0 < 1.224 for the Ld membranes (red data) and 1.224 < c_{wt}/c_0 < 1.273 for the Lo membranes (green data).

the more rigid Lo membranes (Figure 2d). However, because the vesicle volume was reduced by the deflation, the vesicle shapes had an *apparent* area A_{app} that was smaller than the initial vesicle area A_0. As shown in Figure 3a, this apparent area decreased by about 7%, 3%, and 2.5% during the first, second, and third deflation step, respectively. The missing membrane area, $A = A_0 - A_{app}$, was stored in nanotubes that protruded into the vesicle interior.

This tube formation was observed for both types of membranes and for all three vesicle morphologies (Figure 2c,d). For the VM-A and VM-B morphologies, the tubes underwent strong thermally excited undulations and we had to analyze the whole three-dimensional stack of confocal scans in order to estimate the length of the tubes. Examples are provided by the Movies Ld_1 and Ld_2, which display an Ld vesicle after the first and second deflation step, respectively, and

DOI: 10.1021/acsnano.5b05377
ACS Nano 2016, 10, 463−474

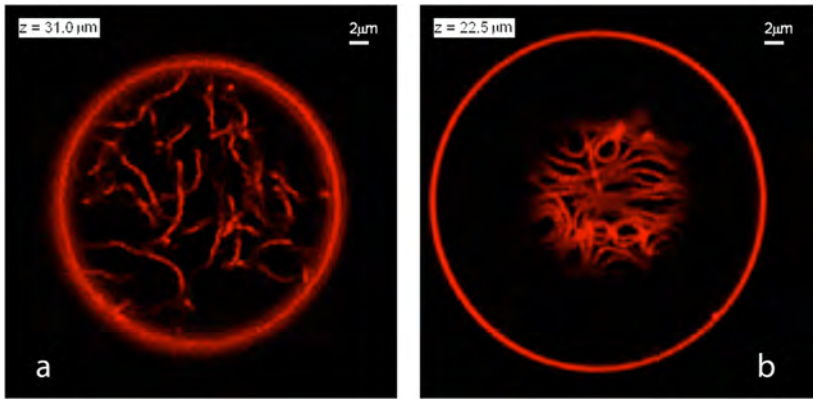

Figure 4. Nanotube patterns within Ld vesicles as observed for the VM-B and VM-C morphologies corresponding to complete and partial wetting of the membranes. (a) Disordered pattern corresponding to an *xy* scan (with $z = 31\ \mu m$) of the VM-B morphology after the second deflation step. Because the Ld membrane is completely wetted by the PEG-rich phase, the nanotubes explore the whole PEG-rich droplet but stay away from the dextran-rich phase. (b) Layer of densely packed tubes as visible in an *xy* scan (with $z = 22.5\ \mu m$) of the VM-C morphology after the fourth deflation step. As a result of partial wetting, the nanotubes now adhere to the pd interface between the two aqueous droplets and form a thin layer in which crowding leads to short-range orientational order of the tubes. Note that the tube layer is only partially visible because the pd interface is curved into a spherical cap.

reveal that the Ld tubes were quite long, of the order of 20 μm. For the VM-C morphologies, longer tube segments can be recognized in a single image because the tubes were then localized close to the pd interface between the PEG-rich and the dextran-rich droplet, see Movie Ld_4. This localization is a direct consequence of partial membrane wetting which favors adhesion of the tubes to the pd interface. Thus, the complete-to-partial wetting transition can be directly deduced from the observed remodelling of the nanotubes which explore the whole PEG-rich droplet for the VM-B but adhere to the pd interface for the VM-C morphology, see Figure 4.

Because the deflation path was close to the critical consolute point, the tension Σ_{pd} of the pd interface was rather low and varied between 0.1 and 10 μN/m, see Figure 3b. For the VM-C morphology, *i.e.*, for partial wetting of the membranes by the two phases, the pd interface forms a contact line with the membrane and the resulting geometry can be characterized by effective contact angles as defined in Figure S3. The variation of these contact angles with the osmotic deflation is displayed in Figure 3c.

Nucleation and Growth of Necklace-like Tubes. The tubes of the Lo membranes were sufficiently thick to determine their shapes directly from the confocal images. The three-dimensional scans in the Movies Lo_1 and Lo_2 show that each Lo vesicle contains many necklace-like tubes consisting of quasi-spherical membrane beads connected by thin membrane necks. The presence of these tubes can be understood from the competition of two kinetic pathways which are related to two different bifurcations of the vesicle shape. Initial deflation of a spherical vesicle leads, *via* an oblate-stomatocyte bifurcation,[26] to the formation of a single spherical bud protruding into the vesicle interior, corresponding to the shape L^{sto} in Figure 5. Upon further volume reduction, the vesicle can follow two alternative pathways depending on the lipid flow through the narrow membrane neck between the bud and the mother vesicle. If this flow is relatively fast, the bud grows in size until it transforms, *via* a sphere-to-prolate bifurcation, into a short necklace of two identical spheres, corresponding to the shape $L^{[2]}$ in Figure 5.

As we continue to deflate the vesicle, the "fast-flow" pathway acts to elongate the necklace-like tube which then passes through the necklace-like shapes $L^{[n]}$ that consist of an increasing number n of small spheres connected by thin membrane necks, see Figure 5. The energy landscape in Figure 5a and the tube shapes in Figure 5b have been obtained by minimizing the bending energy of the membrane, see Methods and Section S1. On the other hand, if the lipid flow through the neck is relatively slow or blocked, the mother vesicle uses the released excess area to form a second bud. Therefore, the deflation of the vesicle generates new buds *via* the "slow-flow" pathway which are then elongated into necklace-like tubes *via* the "fast-flow" pathway.

Necklace–Cylinder Coexistence and Critical Tube Length. Even though the vast majority of the Lo tubes were necklace-like, we also observed cylindrical tubes for the VM-C morphology of Lo membranes. Somewhat surprisingly, both necklace-like and cylindrical tubes were found to coexist on the same vesicle. One example is provided by the Lo_4 vesicle displayed in Figure 6 and Movie Lo_4. Close inspection of these confocal images reveals the existence of two long cylindrical tubes that spiral around the spherical cap of the pd interface. These observations can be understood from the competition of different energy contributions which favor necklace-like tubes below a certain critical tube length and cylindrical tubes above this length. At the critical tube length, the necklace-like tube transforms into a cylindrical one. Such a transformation can proceed in a continuous manner *via* intermediate unduloids as shown in Figure 7.

For the VM-A and VM-B morphologies, the existence of a critical tube length can be understood intuitively from the following simple argument. A necklace-like tube consisting of small spheres with radius $R_{ss} = 1/|m|$ as depicted in Figure 7a has vanishing bending energy. The main body of a cylindrical tube with radius $R_{cy} = 1/(2|m|)$ as displayed in Figure 7c also has vanishing bending energy, but the cylinder must be closed by two end-caps which have a finite bending energy. Therefore, the bending energy of the membrane disfavors the cylindrical tube. On the other hand, the necklace-like tube has a larger volume compared to the cylindrical one and the osmotic pressure difference across the membranes acts to compress the tubes when they protrude into the interior solution inside the vesicles.[8] Therefore, such a tube can lower its energy by

DOI: 10.1021/acsnano.5b05377
ACS Nano 2016, 10, 463–474

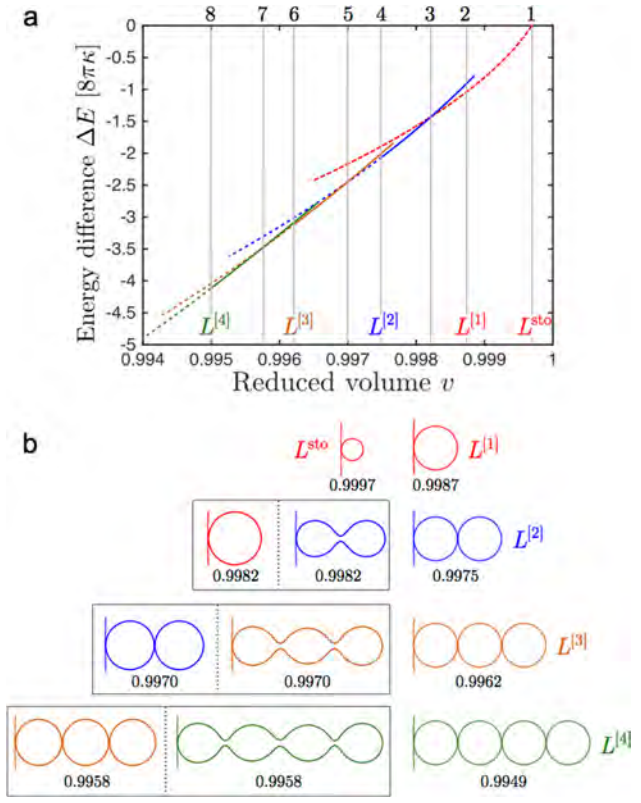

Figure 5. Formation and growth of necklace-like tube. (a) Energy landscape with different branches of equilibrium shapes as a function of the reduced vesicle volume v. The latter volume has the value $v = 1$ for a spherical shape and continuously decreases during deflation, see Methods. The energy difference ΔE describes the deflation-induced reduction in bending energy compared to the initial spherical vesicle. The eight vertical lines labeled from 1 to 8 (top) describe eight discrete deflation steps. (b) Shapes of necklace-like tube corresponding to the eight vertical lines in panel a. The short vertical line on the left end of the tubes corresponds to a short segment of the mother vesicle which is connected to each tube by a thin membrane neck. As we deflate the initial vesicle with $v = 1$, we move along the 1-necklace branch (red) that begins at the limit shape L^{sto} with bead radius $R_{ss} \approx 1/(2|m|)$ and $v = 0.9997$. After passing the shape $L^{[1]}$ with $R_{ss} = 1/|m|$ and $v = 0.9987$, we reach the reduced volume $v = 0.9982$ at which the 1-necklace branch crosses the 2-necklace branch (blue). For the latter v-value, a 1-necklace coexists with an open 2-necklace. Further deflation leads to the 2-necklace $L^{[2]}$ with a closed neck at $v = 0.9975$ and, subsequently, to the 3-necklace branch (orange) and the 4-necklace branch (green). The dashed and solid segments of the free energy landscape in panel a correspond to tubes with closed and open necks, respectively. The parameters used in this example belong to the Lo_1 vesicle with size $R_0 = 20.7\ \mu m$ and spontaneous curvature $m = -1.67\ \mu m^{-1}$ as obtained from the area partitioning analysis.

reducing its volume which favors the cylindrical tube. The volume work is proportional to the tube length whereas the bending energy of the end-caps is independent of this length. It then follows from the competition between these two energies that short tubes are necklace-like whereas long tubes are cylindrical.

The same conclusion is obtained from the systematic theory in Section S1 which predicts that an individual necklace-like tube transforms into a cylindrical one when the length of the necklace reaches the critical value L^*_{tu} and that this critical length lies within the interval $2.84\ R_0 < L^*_{tu} < 3R_0$ for the observed VM-A and VM-B morphologies where $R_0 \equiv \sqrt{A_0/(4\pi)}$ represents the radius of the initial vesicle with area A_0. The upper bound $3R_0$ for the critical tube length is universal and applies to a vesicle with a single tube, whereas the lower bound $2.84R_0$ applies to a vesicle with an arbitrary number of tubes and follows from the observed reduction of the apparent vesicle area during the first two deflation steps. The critical tube area of a single tube is then given by $2\pi L^*_{tu}/|m|$ which is about $6\pi R_0/|m|$. These bounds for the VM-A and VM-B morphologies agree with the observed necklace-like shapes of the Lo tubes which are all shorter than the critical tube length. The Ld tubes are about 5 times longer than the Lo tubes, but they are still shorter than the critical tube length. On the basis of the latter observation and the high flexibility of the Ld tubes, see further below, we conclude that the Ld tubes for the VM-A and VM-B morphologies have a necklace-like shape as well.

For the VM-C morphology, the nanotubes adhere to the pd interface. In this case, the critical tube length is determined by the interplay between (i) the adhesion energy which is proportional to tube length and favors the cylindrical tube and (ii) the bending energy of the end-caps for the cylindrical tube which disfavors the latter tube. The systematic theory in Section S2 now leads to a critical tube length L^*_{ad} that depends on four material parameters, namely the bending rigidity, the spontaneous curvature, the interfacial tension of the pd interface, and the intrinsic contact angle, as described by eq S47 and Figure S4. All of these parameters have been determined experimentally and two of them are found to vary significantly along the deflation path which implies a corresponding variation of the critical tube length L^*_{ad}. The values for the Ld_4 and the Lo_4 vesicle, for example, are given by 5.6 and 21.4 μm, respectively (Figure S4d). The latter value agrees with the length of the cylindrical tubes as observed for the Lo membranes. When we compare the length of individual tubes in Movie Ld_4 with the critical length of 5.6 μm, we conclude that the Ld tubes have a cylindrical shape for this VM-C morphology.

Spontaneous Curvature from Image Analysis. For the Lo membranes, the spontaneous curvature can be directly estimated from the shape of the tubes. As mentioned, all Lo tubes found for the VM-A and VM-B morphologies were relatively short and necklace-like which implies that the spontaneous curvature can be estimated *via* $m = -1/\langle R_{ss}\rangle$ with the average radius $\langle R_{ss}\rangle$ of the small, quasi-spherical beads. For the Lo_1 vesicle after the first deflation step, for example, this direct shape analysis leads to $\langle R_{ss}\rangle = 0.72\ \mu m$ and to the spontaneous curvature $m = -1.4\ \mu m^{-1}$. All m-values obtained in this manner are displayed in Figure 8a as green stars. These values have an accuracy of about 20%, reflecting the relative standard deviation of the measured bead radius R_{ss}.

The direct shape analysis was also applied to the cylindrical and necklace-like tubes coexisting on the Lo_4 vesicle, see Figure 6. The average diameter $\langle 2R_{cy}\rangle$ of the cylindrical tubes as obtained from the confocal scans (Figure 6d,e) implies the spontaneous curvature $m = -1/\langle 2R_{cy}\rangle$ which leads to $m = -1.82\ \mu m^{-1}$ for the cylindrical tubes on the Lo_4 vesicle, with an accuracy of about ±13% corresponding to the relative standard deviation of the measured diameter of the cylinders (Figure 6f). For the latter vesicle, the average bead diameter of the necklace-like tubes leads to $m = -1.56\ \mu m^{-1}$ with an accuracy of about ±19% (Figure 6g). The good agreement

DOI: 10.1021/acsnano.5b05377
ACS Nano 2016, 10, 463−474

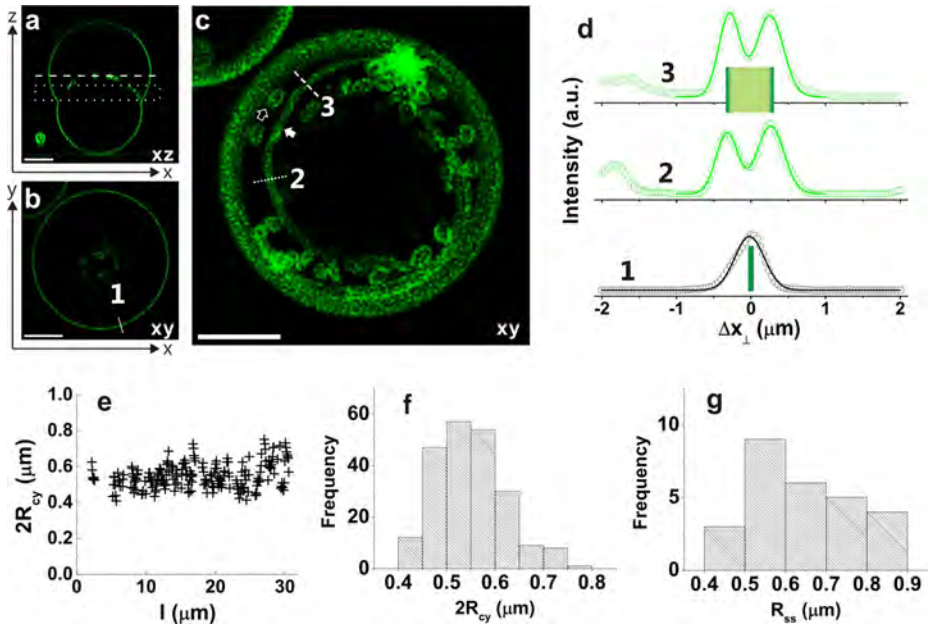

Figure 6. Necklace-cylinder coexistence on Lo_4 vesicle: (a) confocal *xz*-scan; (b) confocal *xy*-scan at $z = 29\ \mu$m corresponding to the dashed line in panel a; (c) superposition of 6 confocal *xy*-scans at $z = 20$, 21, 22, 23, 24, and 25 μm from Movie Lo_4, corresponding to the dotted rectangle in panel a. This superposition reveals the coexistence of two long cylindrical tubes and several short necklace-like tubes, see also Movie Lo_4. All scale bars are 10 μm. (d) Fluorescent intensity along the solid white line 1 in panel b perpendicular to the GUV contour and along the dotted and dashed white lines 2 and 3 in panel c across a cylindrical tube. The quantity $\Delta x_\perp$ is the coordinate perpendicular to the GUV contour or membrane tube. The intensity profiles can be well fitted by Gaussian distributions with a half-peak width of $0.35 \pm 0.05\ \mu$m. The peak−peak separations for the lines 2 and 3 lead to the estimated tube diameters $2R_{cy} = 0.58$ and 0.54 μm, respectively. (e) The tube diameter $2R_{cy}$ as a function of tube position, where l is the distance from the top end of the tube. (f) Cylindrical tubes: histogram of tube diameters $2R_{cy}$ with average tube diameter $\langle 2R_{cy}\rangle = 0.55\ \mu$m, standard deviation $\sigma_{cy} = 0.07\ \mu$m, and relative standard deviation $\sigma_{cy}/\langle 2R_{cy}\rangle = 0.13$. (g) Necklace-like tubes: histogram of bead radii R_{ss} with average bead radius $\langle R_{ss}\rangle = 0.64\ \mu$m, standard deviation $\sigma_{ss} = 0.12\ \mu$m, and relative standard deviation $\sigma_{ss}/\langle R_{ss}\rangle = 0.19$. Therefore, the direct shape analysis of the cylindrical and necklace-like tubes leads to the estimates $m = -1/(2R_{cy}) = -1.82 \pm 0.24\ \mu\text{m}^{-1}$ and $m = -1/R_{ss} = -1.56 \pm 0.30\ \mu\text{m}^{-1}$.

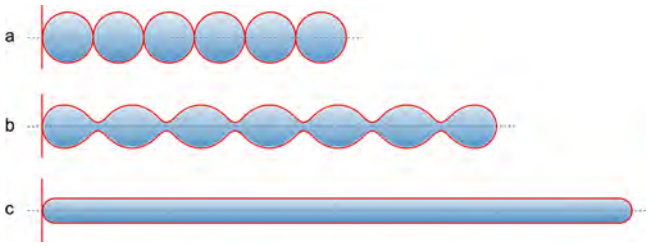

Figure 7. Low energy transformation of a necklace-like tube into a capped cylinder: all three tubes have the same surface area and, apart from the end-caps, the same mean curvature M which is equal to the spontaneous curvature m. (a) Necklace-like tube $L^{[6]}$ with vanishing bending energy consisting of six spherical beads connected by thin membrane necks. The small spheres have radius $R_{ss} = 1/|m|$ and mean curvature $M = -1/R_{ss} = m$. (b) Capped unduloid with neck radius R_{ne}, bulge radius R_{bu}, and mean curvature $M = -1/(R_{ne} + R_{bu}) = m$. (c) Capped cylinder with radius $R_{cy} = 1/(2|m|)$ and mean curvature $M = -1/(2R_{cy}) = m$. The transformation of the sphere-necklace into the cylinder proceeds *via* a continuous family of intermediate unduloids. During this transformation, the tube volume is reduced by a factor 3/4. Apart from their end-caps, the unduloids and the cylinder have the same bending energy as the sphere-necklace. All curvatures are negative because the tubes protrude into the interior aqueous compartments of the vesicles.

between the m-values obtained from the cylindrical and necklace-like tubes justifies our implicit assumption that the spontaneous curvature is uniform along the whole membrane of the vesicle.

For the Ld membranes, we could not resolve the shapes of the nanotubes because they had a thickness below optical resolution. However, we could still deduce the spontaneous curvature from two geometric quantities that can be directly determined from the confocal scans: the total tube area $A = A_0 - A_{app}$ and the total tube length L. The latter length can be directly estimated from the three-dimensional confocal scans, see Movies Ld_j, with an uncertainty of about ±15%. Indeed, all tubes with constant mean curvature are then characterized by spontaneous curvatures within the interval $-2\pi L/A \le m \le -\pi L/A$ (Figure S5). Furthermore, if a fraction Λ of the total tube length is cylindrical and the remaining fraction $1 - \Lambda$ is necklace-like, we obtain the estimate

$$m = -(2 - \Lambda)\frac{\pi L}{A} = -(2 - \Lambda)\frac{\pi L}{A_0 - A_{app}} \quad \text{(area partitioning)} \tag{1}$$

For the VM-A and VM-B morphologies of the Lo membranes, all tubes had a necklace-like shape which implies $\Lambda = 0$. After the first deflation step of the Lo vesicle, for example, we measured the excess area $A = 354\ \mu\text{m}^2$ and the overall tube length $L = 94\ \mu$m which leads, *via* eq 1 with $\Lambda = 0$, to the spontaneous curvature $m = -1.67\ \mu\text{m}^{-1}$. For the VM-C morphologies, on the other hand, tube adhesion can lead to some cylindrical tubes and nonzero Λ-values (Table S2). The m-values obtained *via* eq 1 are displayed in Figure 8a as green

DOI: 10.1021/acsnano.5b05377
ACS Nano 2016, 10, 463−474

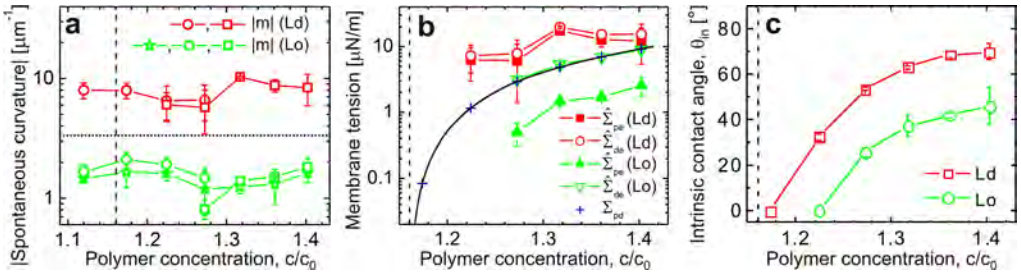

Figure 8. Variation of deduced membrane parameters with osmotic deflation: in all panels, the red and green data correspond to the Ld and Lo membranes, respectively, and the vertical dashed line to the critical concentration c_{cr}. (a) Absolute value of the spontaneous curvature in contact with the uniform aqueous phase (data for $c/c_0 = 1.120$) and with the PEG-rich aqueous phase (data for $c/c_0 \geq 1.174$). The data were obtained by direct shape analysis of the nanotubes (green stars), area partitioning analysis as given by eq 1 (open circles), and force balance analysis described by eq 2 (open squares). The horizontal dotted line corresponds to the optical resolution limit of 1/(300 nm). (b) Membrane tensions $\hat{\Sigma}_{pe}$ and $\hat{\Sigma}_{de}$ within the pe (p, PEG-rich phase; e, exterior phase) and de (d, dextran-rich phase; e, exterior phase) membrane segments separating the external medium from the PEG-rich and dextran-rich phase within the vesicle as defined in Figure S3b. For comparison, the interfacial tension Σ_{pd} is also included (blue crosses and solid black line). (c) Intrinsic contact angle θ_{in} between the pd interface and the vesicle membrane as defined in Figure S3c. The intrinsic contact angle is obtained from the effective contact angles *via* $\cos(\theta_{in}) = [\sin(\theta_p) - \sin(\theta_d)]/\sin(\theta_e)$.[28] Note that the intrinsic contact angle, which represents a material parameter, varies rather smoothly with the polymer concentration, in contrast to the effective contact angles in Figure 3c.

open circles and have an accuracy of ±15%, the main uncertainty arising from the measurement of the tube length L.

For the Ld tubes, we could not estimate the fraction Λ from the confocal scans. However, the high flexibility of these tubes as observed for the VM-A and VM-B morphologies provides strong evidence that these tubes were necklace-like as well. The tube flexibility can be characterized by the persistence length for tube bending. Using the parameter values for the Ld membranes, we then find that a cylindrical tube has a persistence length of 15 μm (Section S3), whereas the persistence length of the corresponding necklace-like tube should be comparable to the diameter of the small spheres. Inspection of the Movies Ld_1 and Ld_2 reveals that the thermal fluctuations of the Ld tubes lead to hairpin-like conformations with curvature radii of the order of 2 μm which implies a persistence length below 2 μm. Such an upper bound for the persistence length is consistent with a necklace-like but not with a cylindrical tube morphology. As mentioned, the same conclusion is obtained from the observed tube lengths which are shorter than the critical tube lengths for the necklace-cylinder transformation. Therefore, we estimated the spontaneous curvatures for the VM-A and VM-B morphologies of the Ld membranes using eq 1 with $\Lambda = 0$. The spontaneous curvature of the Ld_1 vesicle, for example, is then found to be $m = -1/(125\ \text{nm})$. For the VM-C morphologies of the Ld membranes, we deduced the total tube length L from the density of the tubes at the pd interface and estimated the spontaneous curvature *via* eq 1 using the value $\Lambda = \frac{1}{2} \pm \frac{1}{2}$, thereby taking the whole range $0 \leq \Lambda \leq 1$ of possible Λ-values into account.

For the VM-C morphologies of both the Lo and the Ld membranes, the values of the spontaneous curvature as deduced from the direct shape and the area partitioning analysis could be validated *via* a third, completely different mode of analysis. The latter mode is based on the interfacial tension Σ_{pd} of the pd interface (Figure 3b) as well as on the effective contact angles (Figure 3c).[7] Using these quantities and the force balance along the contact line, we computed the membrane tensions in the two segments (Figure 8b) and the spontaneous curvature *via*

$$m = -\left(\frac{\Sigma_{pd}}{2\kappa}\frac{\sin(\theta_d)}{\sin(\theta_e)}\right)^{1/2} \quad \text{(force balance)} \tag{2}$$

With the use of the measured bending rigidities for the Ld and Lo membranes, the expression given by eq 2 leads to m-values that are in good agreement with those obtained *via* the two other modes of analysis, see open squares in Figure 8a.

Spontaneous Curvature Generated by PEG Adsorption. Because vesicle tubulation was only observed in the presence of the polymers, the spontaneous curvature of the vesicle membranes must arise from the polymer-membrane interactions. If these interactions are effectively attractive or repulsive, the polymers form adsorption or depletion layers on the two bilayer leaflets. The membrane then prefers to bulge toward the solutions with the higher and lower concentrations for polymer adsorption and depletion, respectively.[29] After the first deflation step, both the PEG and the dextran concentrations in the interior aqueous solution are larger than in the exterior solution (Figure 2a). After the second and all subsequent deflation steps, the PEG concentration in the interior PEG-rich phase is again larger than in the exterior solution, but the dextran concentration in the interior phase is now smaller than in this exterior solution (Figure 2a). Furthermore, all deflation steps lead to a negative spontaneous curvature of the membranes. These observations are only consistent with the theoretical results in ref 29 if the spontaneous curvature is induced by PEG adsorption. The latter conclusion has been confirmed by additional experiments in which we used the same lipid composition but exposed the vesicles to aqueous solutions that contained only PEG and no dextran, see Figure 9. For the latter systems, osmotic deflation of the vesicles again generated membrane nanotubes that protruded into the solution with the higher PEG concentration.

To corroborate these conclusions about PEG adsorption and to obtain direct insight into the conformations of the adsorbed PEG molecules, we performed molecular dynamics simulations of the polymer−lipid systems with atomistic resolution for the experimentally used lipid compositions and chain length of PEG, see Methods. Typical conformations of adsorbed chains are displayed in Figure 10a,b for both Ld and Lo membranes. These conformations indicate that the PEG molecules are only

DOI: 10.1021/acsnano.5b05377
ACS Nano 2016, 10, 463−474

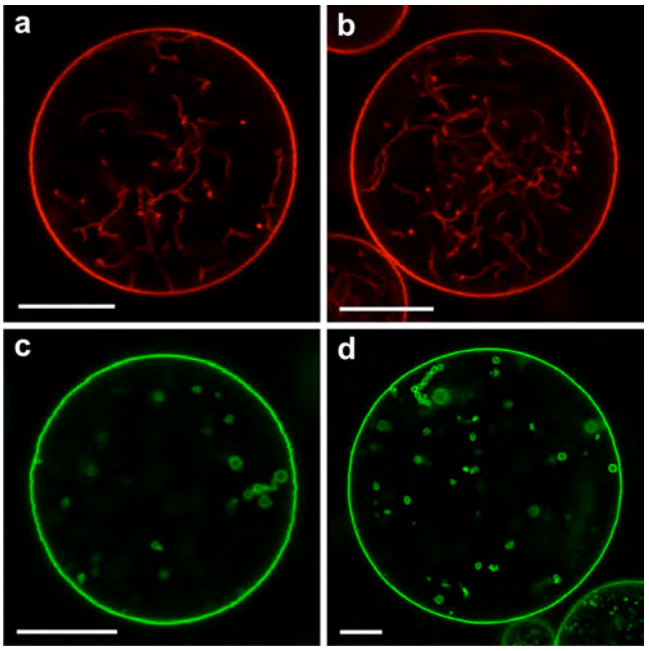

Figure 9. Nanotubes formed in Ld (red) and Lo (green) vesicles exposed to aqueous solutions of PEG and sucrose, *i.e.*, in the absence of dextran. The interior solution contained only PEG and no sucrose with the initial weight fraction w_p = 0.0443. The vesicles were deflated by exchanging the external medium by a hypertonic solution with no PEG but an increasing weight fraction w_{su} of sucrose. The vesicles in (a) and (c) are obtained for w_{su} = 0.0066, those in (b) and (d) for w_{su} = 0.01. The corresponding osmolarity ratios P_e/P_0 are 1.05 and 1.61, respectively. The white scale bars are 10 μm in all panels.

weakly bound, with relatively short contact segments (or "trains"), and relatively long loops in between. The two terminal OH groups of the PEG molecule were frequently bound to the membrane *via* hydrogen bonds. In addition, a small number of contacts was formed between the polymer backbones and the membranes. Combining both types of contacts, the adsorbed polymers formed an average number of 4.5 ± 2.3 and 3.2 ± 2.1 contacts with the Ld and the Lo membranes, respectively. A more quantitative measure for the affinity of the polymers to the membranes is provided by the potentials of mean force displayed in Figure 10c,d. These potentials indicate that the PEG molecules have essentially the same affinity for both types of membranes, with a binding free energy of about 4 kJ/mol or 1.6 k_BT per polymer chain.

Discussion of Deduced Spontaneous Curvatures. The spontaneous curvatures displayed in Figure 8a have two remarkable features: (i) they depend only weakly on the total polymer concentration c within the vesicles; and (ii) when exposed to the same asymmetric environment, the spontaneous curvature of the Ld membrane is about 4.7 times larger than that of the Lo membrane. The second feature is relatively easy to explain. Indeed, the spontaneous curvature generated by adsorption is theoretically predicted to be inversely proportional to the bending rigidity of the membrane[8,29] as recently confirmed for the adsorption of small molecules by molecular dynamics simulations.[30] If we assume that the PEG chains have similar affinities to the Ld and Lo membranes as implied by our simulation results (Figure 10c,d), the ratio m_{Ld}/m_{Lo} of the spontaneous curvatures should be equal to the ratio κ_{Lo}/κ_{Ld} of the bending rigidities. The latter rigidity ratio is estimated to be $\kappa_{Lo}/\kappa_{Ld} \simeq 4.5$, based on the experimental results in ref 25, which should be compared with the curvature ratio $m_{Ld}/m_{Lo} \simeq 4.7$ in Figure 8a. Because the experimental uncertainty is of the order of 10 to 20% for both ratios, the data are consistent with $m_{Ld}/m_{Lo} \simeq \kappa_{Lo}/\kappa_{Ld}$ and, thus, with a comparable amount of adsorbed polymers on both types of membranes, in agreement with our simulation results.

The weak dependence of the spontaneous curvatures on the polymer concentration c within the vesicles is more difficult to understand. Because the polymer weight fractions in the exterior solution were kept constant during all deflation steps, the concentration-dependence of the spontaneous curvatures follows from the concentration-dependence of the PEG coverage on the inner membrane leaflets in contact with the interior polymer solutions. If these leaflets were in contact with *dilute* PEG solutions, the polymer density within the adsorption layer would be increased by a factor of about $\exp[\Delta F_{ch}/k_BT] \simeq 5$ compared to the bulk density, based on the binding free energy $\Delta F_{ch} \simeq 1.6\ k_BT$ for a single PEG chain (Figure 10c,d). Therefore, as the polymer concentration within the interior solution is increased, the PEG coverage on the interior leaflets of the membranes would also be increased which implied a corresponding increase of the spontaneous curvature.

However, for the deflation path studied here, the PEG–dextran solutions were not dilute but semidilute, with substantial overlaps between the chains, see Table S3, which led to repulsive PEG–dextran interactions in the one-phase region and to repulsive PEG–PEG interactions in the PEG-rich phase. When the PEG chains are adsorbed onto the inner leaflet, the local PEG concentration is increased and the PEG chains must experience even more repulsive PEG–PEG and PEG–dextran interactions than in the bulk solutions. For adsorption onto solid surfaces, repulsive chain–chain interactions typically lead to a saturation of the polymer coverage as observed in many experiments, see, e.g., refs 31–33. In the present context, such a saturation of the PEG coverage is quite plausible after the third deflation step. Furthermore, after the first and the second deflation step, the interior polymer solutions were rather close to the critical consolute point with $\epsilon \equiv |c - c_{cr}|/c_{cr}$ of the order of 10^{-2} (Table S3). In such a situation, the correlation length for compositional fluctuations is expected to be large compared to the size of the PEG chains which implies a thickening of the adsorption layers and a corresponding increase in the PEG coverage on the inner membrane leaflets. Thus, the weak concentration-dependence of this coverage should arise from the antagonistic effects of near-critical fluctuations and repulsive chain–chain interactions along the chosen deflation path.

CONCLUSIONS

In summary, we have shown that both Ld and Lo membranes form nanotubes when their leaflets are exposed to two aqueous polymer solutions that differ in their composition. The total length of the tubes is controlled by the osmotic deflation, while their thickness directly reflects the bilayer asymmetry of the membranes as described by their spontaneous curvature. The vast majority of individual Lo nanotubes had a necklace-like shape (Figure 2 as well as Figure S2 and Movies), but we also observed long cylindrical tubes coexisting with shorter necklace-like tubes on the same vesicle (Figure 6 and Movie Lo_4). The formation of many necklace-like tubes can be understood from the competition of two kinetic pathways. The first pathway nucleates new buds of the mother vesicle whereas

DOI: 10.1021/acsnano.5b05377
ACS Nano 2016, 10, 463–474

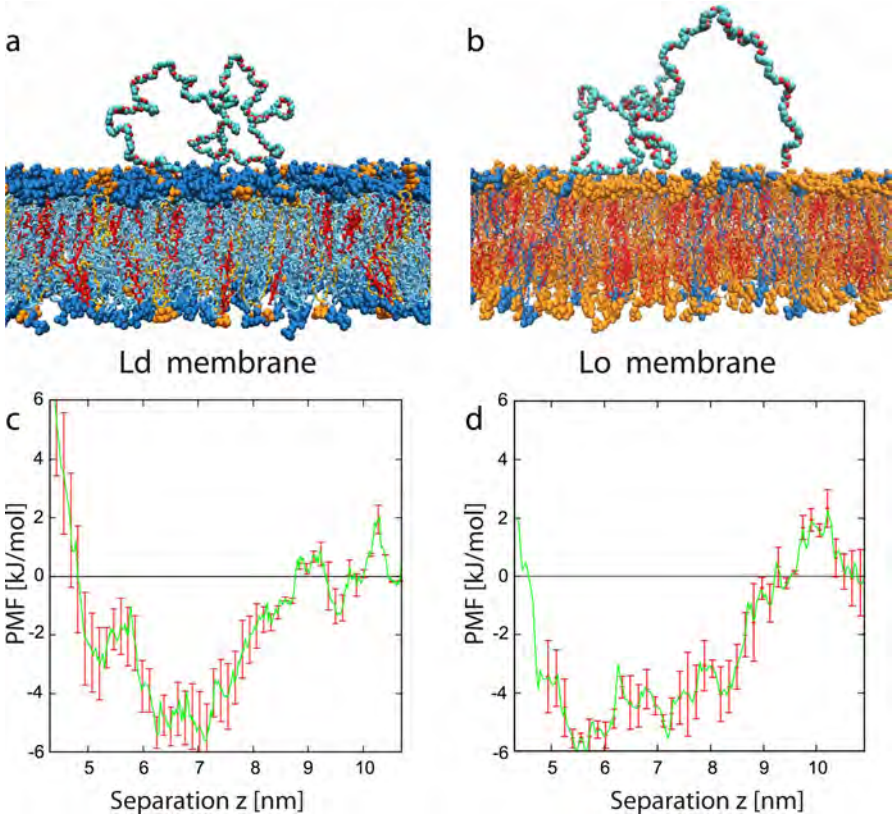

Figure 10. Typical conformation and potential of mean force for adsorbed PEG molecules. (a and b) Simulation snapshots of PEG molecule adsorbed onto Ld and Lo bilayer. The Ld and Lo composition is the same as in Figure 2. The color code for the lipids is blue for DOPC, orange for DPPC, and red for cholesterol. The PEG molecules consist of 180 monomers corresponding to the average molecular weight used in the experiments. Each lipid membrane is immersed in about 27 000 water molecules (not shown). (c and d) Potential of mean force (PMF) for Ld and Lo membranes as a function of the separation z between the polymer's center-of-mass and the bilayer's midplane. The potential wells are relatively broad, with a width of about 4 nm, because the polymer end groups can adsorb even for relatively large z-values. The binding free energy of a single PEG chain is about 4 kJ/mol or 1.6 $k_B T$ for both types of membranes.

the second pathway stores additional area in the existing buds and extends these buds into necklace-like tubes (Figure 5b). These necklace-like tubes transform into cylindrical tubes when their length reaches a certain critical length (Sections S1 and S2). It then follows from the magnitude of the critical tube lengths that individual Ld tubes were necklace-like for the VM-A and VM-B morphologies but cylindrical for some of the VM-C morphologies. In the latter case, the tube adhesion led to a reduction of the critical tube length.

To deduce the spontaneous curvature from the observed vesicle morphologies, we used three different and independent methods of image analysis: direct shape analysis (Figure 6), overall partitioning analysis of membrane area (eq 1), and force balance analysis along the contact line of the partially wetted membranes (eq 2). All three analysis methods gave very consistent values for the spontaneous curvature m as summarized in Figure 8a. The spontaneous curvatures of the Ld and Lo membranes were fairly constant over the range of polymer concentrations studied here, with $m_{Ld} \simeq -8\ \mu m^{-1}$ and $m_{Lo} \simeq -1.7\ \mu m^{-1}$ which implies the curvature ratio $m_{Ld}/m_{Lo} \simeq 4.7$.

We also elucidated the molecular mechanism for the generation of the spontaneous curvatures and showed that these curvatures are induced by the weak adsorption of PEG molecules onto the membranes. Indeed, the formation of nanotubes was also observed in the absence of dextran, e.g., when the giant vesicles were exposed to aqueous solutions of PEG alone (Figure 9). In addition, both the typical conformations of the adsorbed polymers and the associated polymer-membrane affinities were determined by atomistic molecular dynamics simulations (Figure 10). The binding free energies were found to be relatively small and similar in size for Ld and Lo membranes, about 4 kJ/mol or 1.6 $k_B T$ per polymer chain. Because of this similarity, the curvature ratio m_{Ld}/m_{Lo} is approximately equal to the rigidity ratio κ_{Lo}/κ_{Ld}.

Our study can be extended in several ways. First, it will be useful to further corroborate our preliminary results for dilute PEG solutions (Figure 9) in order to avoid the added complexity of semidilute polymer mixtures. Second, using other lipid or polymer compositions with different bending rigidities or polymer-membrane affinities, we can easily vary the tube thickness and, in particular, produce thinner and longer nanotubes which should then exhibit a larger fraction of cylinders. Third, using osmotic deflation in combination with micropipette aspiration to shorten the tubes[7] and/or optical tweezers to extend individual tubes, one should be able to directly probe the dynamics of the necklace-cylinder transformation.

Because our deflation-based approach is both simple and general, it can be applied to other membrane systems of interest. One example is provided by synthetic lipid bilayers with two leaflets that have different compositions as recently produced by a variety of preparation methods.[34−38] With the use of similar methods, it should also be possible to produce

DOI: 10.1021/acsnano.5b05377
ACS Nano 2016, 10, 463−474

bilayers of block copolymers with such a compositional asymmetry. Block copolymer bilayers form giant polymersomes[14] which change their shapes in response to osmotic deflation[15,16,39] and can form tubular shapes as well.[11] Furthermore, our approach can also be used to determine the spontaneous curvature arising from the membrane binding of BAR-domain proteins[17,18] and amphipathic peptides.[19]

In the living cell, the membranes are continuously remodelled by the formation of transport vesicles *via* fission and fusion processes. The magnitude of the spontaneous curvature determines whether these remodelling processes are endergonic or exergonic. If the spontaneous curvature is comparable to the inverse size of the transport vesicle, budding is exergonic and fusion is endergonic. One example for the latter situation is provided by clathrin-dependent endocytosis for which the spontaneous curvature plays a pivotal role.[20]

METHODS

Materials. Dextran (400−500 kg/mol) and poly(ethylene glycol) (PEG 8000, 8 kg/mol) were purchased from Sigma-Aldrich. The polydispersity, measured with gel permeation chromatography, was 1.11 for PEG and 1.83 for dextran. The binodal of the polymer solution was determined by cloud-point titration.[22] The critical consolute (or demixing) point was located at a total polymer concentration of 8.12 wt % with a dextran to PEG weight ratio w_d/w_p = 1.25. The interfacial tensions Σ_{pd} between the dextran-rich and PEG-rich phases were measured using a SITE100 spinning drop tensiometer (Krüss) as described in ref 22. Dioleoylphosphatidylcholine (DOPC) and dipalmitoylphosphatidylcholine (DPPC) were purchased from Avanti Polar Lipids and cholesterol from Sigma-Aldrich. Texas Red labeled dihexadecanoyl phosphoethanolamine (DHPE-TR) was purchased from Invitrogen and distearoyl phosphoethanolamine-*N*-[poly(ethylene glycol)2000-*N*′-carboxyfluorescein] (DSPE-PEG-CF) from Avanti Polar Lipids.

Vesicle Preparation and Deflation. Aqueous polymer solutions with initial weight fraction $(w_d, w_p)_0$ = (0.0390, 0.0312) corresponding to composition 0 (blue cross in Figure 2a,b) were encapsulated within giant vesicles with membranes composed of DOPC, DPPC and cholesterol. The latter vesicles were formed using the electroformation method as described elsewhere.[7] The Ld membranes with lipid composition DOPC:DPPC:cholesterol = 64:15:21 were labeled by 0.1 mol % DHPE-TR. The Lo membranes with lipid composition DOPC:DPPC:cholesterol = 13:44:43 were labeled with 0.2 mol % DSPE-PEG-CF. For these two lipid compositions, the bending rigidities were previously studied; we used the values $\kappa_{Ld} = 0.82 \times 10^{-19}$J and $\kappa_{Lo} = 3.69 \times 10^{-19}$J obtained in ref 25. After preparation, the vesicles were transferred into a chamber filled with an isotonic solution with polymer weight fractions $(w_d, w_p)_{0e}$ = (0.0327, 0.0327), corresponding to the green cross in Figure 2a,b. The deflation was done by exchanging the external medium with a hypertonic solution containing the constant polymer weight fractions w_d = 0.0327 and w_p = 0.0327 and an increasing weight fraction of sucrose. These conditions ensured that the vesicles sedimented toward the coverslip at the bottom of the chamber and that the symmetry axis was oriented perpendicular to this coverslip; see Figure 2c,d and Figure S2a,b.

Confocal Microscopy. Vesicles were observed by a confocal microscope (Leica TCS SP5) with a 63× water immersion objective (N.A. = 1.20). The images were deconvoluted by Huygens Professional software (version 4.3.1, Scientic Volume Imaging), and analyzed using home-developed software in Matlab to determine the contours of the mother vesicle and the membrane nanotubes. A complete three-dimensional scan of a vesicle consisted of a stack of 37−82 confocal images that were taken at different separations from the coverslip, see the Movies Ld_j and Lo_j which display scans of Ld and Lo vesicles after the first, second, and fourth depletion step. The analysis of these scans is described in more detail in Figure 6 and Table S2.

Computation of Vesicle Shapes *via* Free Energy Minimization. For the VM-A and VM-B morphologies, the free energy landscapes of the giant vesicles have been determined by minimizing the bending energy of the vesicle membrane for constant membrane area A_0 and deflation-controlled vesicle volume V. The bending energy depends (i) on the shape of the vesicle membrane which is described by its (local) mean curvature M and (ii) on two fluid-elastic parameters, the bending rigidity κ and the spontaneous curvature m.[26,40] The constraints on area and volume are taken into account by two Lagrange multipliers, Σ and ΔP, and by minimizing the shape functional[26]

$$\mathcal{E} = \int \mathrm{d}A 2\kappa(\mathrm{M} - \mathrm{m})^2 + \Sigma A_0 - \Delta P V \tag{3}$$

We used the vesicle size $R_0 \equiv (A_0/4\pi)^{1/2}$ as the basic length scale and the volume-to-area ratio or reduced volume

$$v \equiv V/[(4\pi/3)R_0^3] \leq 1 \tag{4}$$

as the basic control parameter or reaction coordinate, see Sect. S1 for more details. In this way, we obtained the free energy landscape for a giant vesicle with a necklace-like tube as displayed in Figure 5.

For the VM-C morphology, the overall shape of the vesicles can be determined by an appropriate generalization of the shape functional as described in ref 28. The VM-C shape involves the intrinsic contact angle θ_{in} as an additional material parameter, see Figure S3c. In order to study the adhesion of membrane nanotubes to the pd interface, we ignored the relatively small curvature of the pd interface and calculated the free energies for the adhesion of both necklace-like and cylindrical tubes to a planar pd interface. The results of these calculations are described in Section S2 and summarized in Figure S4.

Molecular Dynamics Simulations of PEG Adsorption. For the atomistic simulations, we used the GROMACS software package 4.5.5 with the Berger force field[41] for the lipids and parameters based on the GROMOS 53A6 force field for the polymers.[42] For the PEG 8000 polymer chain, this force field leads to a radius of gyration of 3.43 nm in reasonable agreement with the value 3.83 nm for PEG 8000 as obtained by linear extrapolation from the results in ref 43 and the value 4.05 nm as estimated in ref 22 based on the PEO data in ref 44. Lipid bilayers corresponding to the experimentally used compositions for the Ld and Lo membranes were assembled, together with a single polymer chain of PEG 8000, in a cubic simulation box of size 10.3 × 10.3 × 14.8 nm^3 with periodic boundary conditions in all three spatial directions for the unrestrained simulations, using the charmm membrane builder.[45] The Ld membrane contained 256 DOPC, 60 DPPC, and 84 cholesterol molecules, whereas the Lo membrane consisted of 52 DOPC, 176 DPPC, and 172 cholesterol molecules (Figure 10). The PEG 8000 molecules had a length of 180 monomers. Bilayer and polymer were immersed in 27 080 water molecules as described by the SPC water model. Both the Ld and the Lo membranes were simulated for 700 ns. For the computations of the potentials of mean force in Figure 10c,d, we increased the box size perpendicular to the membrane to 20.5 nm corresponding to 51 758 water molecules and used 12 umbrella windows, each of which was simulated for 100 ns.

ASSOCIATED CONTENT

Supporting Information

The Supporting Information is available free of charge on the ACS Publications website at DOI: 10.1021/acsnano.5b05377.

Additional experimental data (PDF)
Movie Ld_1 (MPG)
Movie Ld_2 (MPG)
Movie Ld_4 (MPG)
Movie Lo_1 (MPG)
Movie Lo_2 (MPG)
Movie Lo_4 (MPG)

DOI: 10.1021/acsnano.5b05377
ACS Nano 2016, 10, 463−474

AUTHOR INFORMATION

Corresponding Author

*E-mail: lipowsky@mpikg.mpg.de.

Notes

The authors declare no competing financial interest.

ACKNOWLEDGMENTS

We thank Halim Kusumaatmaja for stimulating discussions during the initial phase of this project and acknowledge support by the Partner Group Program of the Max Planck Society and the Chinese Academy of Sciences, the National Natural Science Foundation of China (Grant No. 21274147), the German Science Foundation (DFG) *via* IRTG 1524, and the Federal Ministry of Education and Research (BMBF) *via* the consortium MaxSynBio.

REFERENCES

(1) Marchi, S.; Patergnani, S.; Pinton, P. The Endoplasmic Reticulum-Mitochondria Connection: One Touch, Multiple Functions. *Biochim. Biophys. Acta, Bioenerg.* **2014**, *1837*, 461−469.

(2) van Weering, J. R. T.; Cullen, P. J. Membrane-Associated Cargo Recycling by Tubule-Based Endosomal Sorting. *Semin. Cell Dev. Biol.* **2014**, *31*, 40−47.

(3) Westrate, L. M.; Lee, J. E.; Prinz, W. A.; Voeltz, G. K. Form Follows Function: The Importance of Endoplasmic Reticulum Shape. *Annu. Rev. Biochem.* **2015**, *84*, 791−811.

(4) Wang, X.; Gerdes, H.-H. Transfer of Mitochondria via Tunneling Nnotubes Rescues Apoptotic PC12 Cells. *Cell Death Differ.* **2015**, *22*, 1181−1191.

(5) He, K.; Luo, W.; Zhang, Y.; Liu, F.; Liu, D.; Xu, L.; Qin, L.; Xiong, C.; Lu, Z.; Fang, X.; Zhang, Y. Intercellular Transportation of Quantum Dots Mediated by Membrane Nanotubes. *ACS Nano* **2010**, *4*, 3015−3022.

(6) Sowinski, S.; Jolly, C.; Berninghausen, O.; Purbhoo, M. A.; Chauveau, A.; Köhler, K.; Oddos, S.; Eissmann, P.; Brodsky, F. M.; Hopkins, C.; et al. Membrane Nanotubes Physically Connect T Cells over Long Distances Presenting a Novel Route for HIV-1 Transmission. *Nat. Cell Biol.* **2008**, *10*, 211−219.

(7) Li, Y.; Lipowsky, R.; Dimova, R. Membrane Nanotubes Induced by Aqueous Phase Separation and Stabilized by Spontaneous Curvature. *Proc. Natl. Acad. Sci. U. S. A.* **2011**, *108*, 4731−4736.

(8) Lipowsky, R. Spontaneous Tubulation of Membranes and Vesicles Reveals Membrane Tension Generated by Spontaneous Curvature. *Faraday Discuss.* **2013**, *161*, 305−331.

(9) Sorre, B.; Callan-Jones, A.; Manzi, J.; Goud, B.; Prost, J.; Bassereau, P.; Roux, A. Nature of Curvature Coupling of Amphiphysin with Membranes Depends on its Bound Density. *Proc. Natl. Acad. Sci. U. S. A.* **2012**, *109*, 173−178.

(10) Zhu, C.; Das, S. L.; Baumgart, T. Nonlinear Sorting, Curvature Generation, and Crowding of Endophilin N-Bar on Tubular Membranes. *Biophys. J.* **2012**, *102*, 1837−1845.

(11) Robertson, J. D.; Yealland, G.; Avila-Olias, M.; Chierico, L.; Bandmann, O.; Renshaw, S. A.; Battaglia, G. pH-Sensitive Tubular Polymersomes: Formation and Applications in Cellular Delivery. *ACS Nano* **2014**, *8*, 4650−4661.

(12) Tanaka, M.; Critchley, K.; Matsunaga, T.; Evans, S. D.; Staniland, S. S. Fabrication of Lipid Tubules with Embedded Quantum Dots by Membrane Tubulation Protein. *Small* **2012**, *8*, 1590−1595.

(13) Albertsson, P. A. *Partition of Cell Particles and Macromolecules: Separation and Purification of Biomolecules, Cell Organelles, Membranes, and Cells in Aqueous Polymer Two-Phase Systems and Their Use in Biochemical Analysis and Biotechnology*, 3rd ed.; Wiley, 1986.

(14) Discher, B. M.; Won, Y.-Y.; Ege, D. S.; Lee, J. C.-M.; Bates, F. S.; Discher, D. E.; Hammer, D. A. Polymersoms: Tough Vesicles Made from Diblock Copolymers. *Science* **1999**, *284*, 1143−1146.

(15) Salva, R.; Meins, J.-F. L.; Sandre, O.; Brulet, A.; Schmutz, M.; Guenoun, P.; Lecommandoux, S. Polymersome Shape Transformation at the Nanoscale. *ACS Nano* **2013**, *7*, 9298−9311.

(16) Thiele, J.; Chokkalingam, V.; Ma, S.; Wilson, D. A.; Huck, W. T. S. Vesicle Budding from Polymersomes Templated by Microfuidically Prepared Double Emulsions. *Mater. Horiz.* **2014**, *1*, 96−101.

(17) McMahon, H. T.; Gallop, J. L. Membrane Curvature and Mechanisms of Dynamic Cell Membrane Remodelling. *Nature* **2005**, *438*, 590−596.

(18) Rao, Y.; Haucke, V. Membrane Shaping by the Bin/Amphitaphysin/Rvs (BAR) Domain Protein Superfamily. *Cell. Mol. Life Sci.* **2011**, *68*, 3983−3993.

(19) Arouni, A.; Kiessling, V.; Tamm, L.; Dathe, M.; Blume, A. Morphological Changes Induced by the Action of Antimicrobial Peptides on Supported Lipid Bilayers. *J. Phys. Chem. B* **2011**, *115*, 158−167.

(20) Agudo-Canalejo, J.; Lipowsky, R. Critical Particle Sizes for the Engulfment of Nanoparticles by Membranes and Vesicles with Bilayer Asymmetry. *ACS Nano* **2015**, *9*, 3704−3720.

(21) Helfrich, M.; Mangeney-Slavin, L.; Long, M.; Djoko, K.; Keating, C. Aqueous Phase Separation in Giant Vesicles. *J. Am. Chem. Soc.* **2002**, *124*, 13374−13375.

(22) Liu, Y.; Lipowsky, R.; Dimova, R. Concentration Dependence of the Interfacial Tension for Aqueous Two-Phase Polymer Solutions of Dextran and Polyethylene Glycol. *Langmuir* **2012**, *28*, 3831−3839.

(23) Veatch, S.; Keller, S. Separation of Liquid Phases in Giant Vesicles of Ternary Mixtures of Phospholipids and Cholesterol. *Biophys. J.* **2003**, *85*, 3074−3083.

(24) Tian, A.; Capraro, B. R.; Esposito, C.; Baumgart, T. Bending Stiffness Depends on Curvature of Ternary Lipid Mixture Tubular Membranes. *Biophys. J.* **2009**, *97*, 1636−1646.

(25) Heinrich, M.; Tian, A.; Esposito, C.; Baumgart, T. Dynamic Sorting of Lipids and Proteins in Membrane Tubes with a Moving Phase Boundary. *Proc. Natl. Acad. Sci. U. S. A.* **2010**, *107*, 7208−7213.

(26) Seifert, U.; Berndl, K.; Lipowsky, R. Shape Transformations of Vesicles: Phase Diagram for Spontaneous Curvature and Bilayer Coupling Model. *Phys. Rev. A: At., Mol., Opt. Phys.* **1991**, *44*, 1182−1202.

(27) Lipowsky, R. The Conformation of Membranes. *Nature* **1991**, *349*, 475−481.

(28) Kusumaatmaja, H.; Li, Y.; Dimova, R.; Lipowsky, R. Intrinsic Contact Angle of Aqueous Phases at Membranes and Vesicles. *Phys. Rev. Lett.* **2009**, *103*, 238103.

(29) Breidenich, M.; Netz, R.; Lipowsky, R. The Influence of Non-Anchored Polymers on the Curvature of Vesicles. *Mol. Phys.* **2005**, *103*, 3169−3183.

(30) Rózycki, B.; Lipowsky, R. Spontaneous Curvature of Bilayer Membranes from Molecular Simulations: Asymmetric Lipid Densities and Asymmetric Adsorption. *J. Chem. Phys.* **2015**, *142*, 054101.

(31) Felter, R. E.; Ray, L. N. Polymer Adsorption Studies at the Solid-Liquid Interface Using Gel Permeation Chromatography. *J. Colloid Interface Sci.* **1970**, *32*, 349−360.

(32) Voronov, A.; Luzinov, I.; Minko, S.; Sidorenko, A. Adsorption of Polymers at the Surface Concentrations in the Diluted to Semidiluted Regimes. *Macromolecules* **1997**, *30*, 6929−6936.

(33) Liufu, S.; Xiao, H.; Li, Y. Investigation of PEG Adsorption on the Surface of Zinc Oxide Nanoparticles. *Powder Technol.* **2004**, *145*, 20−24.

(34) Hwang, W. L.; Chen, M.; Cronin, B.; Holden, M.; Bayley, H. Asymmetric Droplet Interface Bilayers. *J. Am. Chem. Soc.* **2008**, *130*, 5878−5879.

(35) Chiantia, S.; Schwille, P.; Klymchenko, A. S.; London, E. Asymmetric GUVs Prepared by MbCD-Mediated Lipid Exchange: An FCS Study. *Biophys. J.* **2011**, *100*, L01−L03.

(36) Hu, P. C.; Li, S.; Malmstadt, N. Microfluidic Fabrication of Asymmetric Giant Lipid Vesicles. *ACS Appl. Mater. Interfaces* **2011**, *3*, 1434−40.

(37) Richmond, D. L.; Schmid, E. M.; Martens, S.; Stachowiak, J. C.; Liska, N.; Fletcher, D. A. Forming Giant Vesicles with Controlled

DOI: 10.1021/acsnano.5b05377
ACS Nano 2016, 10, 463−474

Membrane Composition, Asymmetry, and Contents. *Proc. Natl. Acad. Sci. U. S. A.* **2011**, *108*, 9431−6.
(38) Matosevic, S.; Paegel, B. M. Layer-by-Layer Cell Membrane Assembly. *Nat. Chem.* **2013**, *5*, 958−63.
(39) Meeuwissen, S. A.; Kim, K. T.; Chen, Y.; Pochan, D. J.; van Hest, J. C. M. Controlled Shape Transformation of Polymersome Stomatocytes. *Angew. Chem., Int. Ed.* **2011**, *50*, 7070−7073.
(40) Helfrich, W. Elastic Properties of Lipid Bilayers: Theory and Possible Experiments. *Z. Naturforsch.* **1973**, *28c*, 693−703.
(41) Berger, O.; Edholm, O.; Jähnig, F. Molecular Dynamics Simulations of a Fluid Bilayer of Dipalmitoylphosphatidylcholine at Full Hydration, Constant Pressure, and Constant Temperature. *Biophys. J.* **1997**, *72*, 2002−2013.
(42) Fuchs, P. F.; Hansen, H. S.; Hünenberger, P. H.; Horta, B. A. C. A GROMOS Parameter Set for Vicinal Diether Functions: Properties of Polyethyleneoxide and Polyethyleneglycol. *J. Chem. Theory Comput.* **2012**, *8*, 3943−3963.
(43) Bhat, R.; Timasheff, S. N. Steric Exclusion is the Principal Source of the Preferential Hydration of Proteins in the Presence of Polyethylene Glycols. *Protein Sci.* **1992**, *1*, 1133−1143.
(44) Devanand, K.; Selser, J. C. Asymptotic Behavior and Long-Range Interactions in Aqueous Solutions of Poly(ethy1ene oxide). *Macromolecules* **1991**, *24*, 5943−5947.
(45) Wu, E. L.; Cheng, X.; Jo, S.; Rui, H.; Song, K. C.; Davila-Contreras, E. M.; Qi, Y.; Lee, J.; Monje-Galvan, V.; Venable, R. M.; et al. CHARMM-GUI Membrane Builder toward Realistic Biological Membrane Simulations. *J. Comput. Chem.* **2014**, *35*, 1997−2004.

DOI: 10.1021/acsnano.5b05377
ACS Nano 2016, 10, 463−474

Patterns of Flexible Nanotubes Formed by Liquid-Ordered and Liquid-Disordered Membranes - Supporting Information

Yonggang Liu[†,‡], Jaime Agudo-Canalejo[†], Andrea Grafmüller[†], Rumiana Dimova[†] and Reinhard Lipowsky[†*]

[†] *Theory and Bio-Systems, Max Planck Institute of Colloids and Interfaces, Science Park Golm, 14424 Potsdam, Germany*

[‡] *State Key Laboratory of Polymer Physics and Chemistry, Changchun Institute of Applied Chemistry, Chinese Academy of Sciences, 130022 Changchun, China*

November 20, 2015

This Supporting Information contains the following items:

Supporting Sections:
Sect. S1: Critical tube length for VM-A and VM-B morphologies.
Sect. S2: Critical tube length for VM-C morphologies.
Sect. S3: Tube flexibility and persistence length.

Supporting Figures:
Fig. S1: Shapes of aqueous droplets for different vesicle morphologies.
Fig. S2: Vertical cross sections of the Ld and Lo vesicles in Fig. 2.
Fig. S3: Contact angles for VM-C morphologies.
Fig. S4: Adhesion of membrane nanotubes to the pd interface.
Fig. S5: Different tube shapes with the same membrane area and tube length.

Supporting Tables:
Table S1: Deflation path within the phase diagram of Fig. 2.
Table S2: Geometry of deflated Ld_j and Lo_j vesicles.
Table S3: Overlap of PEG and dextran chains along the deflation path.

Captions for the Movies Ld_j and Lo_j with $j = 1, 2, 4$.

References for Supporting Information

S1 Critical tube length for VM-A and VM-B morphologies

S1.1 Giant vesicle with necklace-like tube

Consider a giant vesicle with a spherical shape of radius R_0. The vesicle membrane has a large and negative spontaneous curvature m which favors highly curved membrane segments, in contrast to the small curvature $1/R_0$ of the initial vesicle. When the vesicle volume is reduced by osmotic deflation, the membrane can form an '$\mathcal{N}$-shape' consisting of a large spherical mother vesicle together with a necklace-like tube that protrudes into the vesicle interior. We have determined the $\mathcal{N}$-shapes of minimal bending energy as a function of reduced volume

$$v \equiv \frac{V}{V_0} \leq 1 \quad \text{with} \quad V_0 \equiv \tfrac{4\pi}{3} R_0^3 \tag{S1}$$

where $v = 1$ corresponds to the spherical mother vesicle without a necklace-like tube. The results of the numerical energy minimization, which are based on the shape functional in Eq. 3 of the main text, are displayed in Fig. 5.

The $\mathcal{N}$-shapes of minimal bending energy contain the shapes $L^{[N]}$ for which the necklace consists of N spherical beads with radius $R_{\rm ss} = 1/|m|$, see Fig. 5. Such a necklace-like tube has constant mean curvature $M = m$ and, thus, vanishing bending energy as follows from Eq. 3 of the main text. Furthermore, the mother vesicle has the radius

$$R_N = R_0 \sqrt{1 - \frac{N}{(|m|R_0)^2}} < R_0 \tag{S2}$$

as obtained from the conservation of membrane area which has the form

$$A_0 = 4\pi R_0^2 = 4\pi R_N^2 + N 4\pi |m|^{-2} \,. \tag{S3}$$

The necklace is anchored to the mother vesicle by an ideal membrane neck. The latter neck is formed as one approaches the limit shape $L^{\rm sto}$ from the branch of stomatocytes. [1] Likewise, the $L^{[N]}$-shapes with $N \geq 2$ also represent limit shapes which are obtained from necklace-like tubes with open necks, see Fig. 5. The $L^{[1]}$-shape is special because the necklace consists of a single spherical bead (or bud) which is obtained from the limit shape $L^{\rm sto}$ by increasing the bead radius from $R_{\rm ss} = 1/(2|m|)$ to $R_{\rm ss} = 1/|m|$. The $L^{[N]}$-shapes with $N \geq 2$ contain two types of ideal necks, the anchor neck between the mother vesicle and the first bead as well as the ss-ss necks between the small spheres of the necklace. Both types of membrane necks are stable provided $R_{\rm ss} \geq 1/|m|$ [2] which includes the limiting case $R_{\rm ss} = 1/|m|$ considered here.

The volume of the $L^{[N]}$-shapes is given by

$$V_N = \tfrac{4\pi}{3} R_N^3 - N \tfrac{4\pi}{3} R_{\rm ss}^3 = V_0 \left(\left[1 - \frac{N}{(|m|R_0)^2} \right]^{3/2} - \frac{N}{(|m|R_0)^3} \right) \tag{S4}$$

which decreases monotonically with increasing number N of the small beads. Therefore, the sequence of $L^{[N]}$-shapes provides a possible, low-energy pathway for osmotic deflation as depicted in Fig. 5 in the main text.

Because the bending energy of the necklace-like tube with $R_{\rm ss} = 1/|m|$ vanishes, the bending energy of the $L^{[N]}$-shapes arises from the mother vesicle alone, *i.e.*,

$$\mathcal{E}_{\rm be}\left(L^{[N]}\right) = 8\pi\kappa\,\left(1 - mR_N\right)^2 \tag{S5}$$

which is equivalent to

$$\mathcal{E}_{\rm be}\left(L^{[N]}\right) = 8\pi\kappa\,\left[1 + |m|R_0\sqrt{1 - \frac{N}{(|m|R_0)^2}}\right]^2 . \tag{S6}$$

This energy also decreases monotonically with increasing bead number N, compare Fig. 5.

S1.2 Giant vesicle with cylindrical tube

We now transform the $L^{[N]}$-shapes as considered in the previous section into alternative $C^{[N]}$-shapes for which the necklace-like tubes are replaced by cylindrical ones. For each value of N, we perform this transformation in such a way that *both the membrane area and the vesicle volume are conserved*.

The cylindrical tubes consist of cylinders that are closed by two spherical caps, where one of these end caps is connected to the mother vesicle by an ideal neck. The body of such a cylinder has length $L_{\rm cy}$, radius $R_{\rm cy} = 1/(2|m|)$, and mean curvature $M = m$ which implies that this membrane segment has vanishing bending energy. The radius of the mother vesicle is now denoted by $R_{\rm ls}$. Because the $C^{[N]}$-shape is required to have the same membrane area as the $L^{[N]}$-shape, the length scales $L_{\rm cy}$ and $R_{\rm ls}$ are related *via*

$$R_{\rm ls}^2 + \frac{1}{4|m|}L_{\rm cy} + \frac{1}{4m^2} = R_N^2 + \frac{N}{m^2}\,. \tag{S7}$$

A second relation between these two scales is obtained from the requirement that the $C^{[N]}$-shape and the $L^{[N]}$-shape, which both include the mother vesicle, have the same volume which implies

$$R_{\rm ls}^3 - \frac{3}{16m^2}L_{\rm cy} - \frac{1}{8|m|^3} = R_N^3 - \frac{N}{|m|^3}\,. \tag{S8}$$

When we combine the two relations (S7) and (S8) to eliminate $L_{\rm cy}$, we obtain the implicit equation

$$R_{\rm ls}^3\left(1 + \frac{3}{4|m|R_{\rm ls}}\right) = R_N^3\left(1 + \frac{3}{4|m|R_N}\right) - \frac{N + 1/4}{4|m|^3} \tag{S9}$$

for the mother vesicle radius $R_{\rm ls}$ of the $\mathcal{C}^{[N]}$-shape where R_N can be expressed in terms of R_0 *via* (S2). The implicit equation (S9) directly implies that $R_{\rm ls} < R_N$ for all positive values of N. Therefore, the $\mathcal{C}^{[N]}$-shape has a smaller mother vesicle and the membrane area stored in the cylinder exceeds the area stored in the N-necklace. We now define the parameter ϵ *via*

$$R_{\rm ls} = R_N\,(1-\epsilon) \tag{S10}$$

and consider the limit of large $|m|R_0$, in which we obtain the asymptotic equality

$$\epsilon \approx \frac{N+1/4}{12}\left(\frac{1}{|m|R_0}\right)^3 \quad (\text{large } |m|R_0) \tag{S11}$$

from the implicit equation (S9).

The bending energy of the $C^{[N]}$-shape is equal to

$$\mathcal{E}_{\rm be}\left(C^{[N]}\right) = 8\pi\kappa(1-mR_{\rm ls})^2 + 2\pi\kappa \tag{S12}$$

where the first and the second term represents the energy contributions from the mother vesicle and from the two end caps of the cylinder, respectively.

S1.3 Critical tube length for necklace-cylinder transformation

We now compare the bending energy (S12) of the $C^{[N]}$-shape with the bending energy (S5) of the $L^{[N]}$-shape. The mother vesicle of the $C^{[N]}$-shape has the bending energy $8\pi\kappa(1-mR_{\rm ls})^2$ which is smaller than the bending energy $8\pi\kappa\,(1-mR_N)^2$ of the $L^{[N]}$-shape because $R_{\rm ls} < R_N$ and $|m|R_{\rm ls} \gg 1$. However, the capped cylinder has the bending energy $2\pi\kappa$ whereas the necklace has vanishing bending energy. Therefore, when we transform the $L^{[N]}$-shape into the $C^{[N]}$-shape, we reduce the bending energy of the mother vesicle but increase the bending energy of the tube.

We now define the reduced difference

$$\Delta \equiv \frac{\mathcal{E}_{\rm be}\left(C^{[N]}\right) - \mathcal{E}_{\rm be}\left(L^{[N]}\right)}{8\pi\kappa} \tag{S13}$$

between the bending energies of the $C^{[N]}$- and the $L^{[N]}$-shape, which has the form

$$\Delta = (1+|m|R_{\rm ls})^2 + \tfrac{1}{4} - (1+|m|R_N)^2 \tag{S14}$$

or

$$\Delta = |m|(R_{\rm ls}-R_N)\,[2+|m|(R_{\rm ls}+R_N)] + \tfrac{1}{4} \tag{S15}$$

Replacing $R_{\rm ls}$ by $R_N(1-\epsilon)$, the latter relation becomes

$$\Delta = -\epsilon|m|R_N\,[2+2|m|R_N - \epsilon|m|R_N] + \tfrac{1}{4}\ . \tag{S16}$$

The $L^{[N]}$-shape and the $C^{[N]}$-shape are energetically favored for $\Delta > 0$ and $\Delta < 0$, respectively. The critical bead number N^* and the critical tube length

$$L^*_{\rm tu} = N^* 2R_{\rm ss} = N^* 2/|m| \tag{S17}$$

then follow from $\Delta = 0$.

In the limit of large $|m|R_0$ and small $\epsilon \sim (|m|R_0)^{-3}$, see (S11), we obtain the asymptotic equality

$$\Delta \approx -\frac{N + 1/4}{6|m|R_0} + \frac{1}{4} \tag{S18}$$

which implies the critical tube length

$$L^*_{\rm tu} = N^* 2/|m| \approx 3R_0\,. \tag{S19}$$

It is interesting to note that exactly the same relation for the critical tube length is obtained if one replaces the bending energy contribution from the mother vesicle by the volume work performed on the tube by the pressure difference ΔP which behaves as $\Delta P \approx 4\kappa m^2/R_{\rm ls}$ for large $|m|R_{\rm ls}$ and acts to compress the necklace-like tube which has a larger volume than the cylindrical one. [3]

S1.4 Critical tube lengths for mother vesicle with many tubes

So far, we have explicitly discussed a mother vesicle with a single tube. However, the above considerations can be easily extended to a mother vesicle with several tubes. Indeed, all we have to do is to select one of the tubes and to redefine the membrane area and the membrane volume in an appropriate manner. Thus, let us label the selected tube by the index s and the remaining tubes by the index $r = 1, 2, \ldots$. The selected tube has the area A_s, the remaining tubes have the areas A_r. The redefined membrane area $\hat{A}_0$ is then given by

$$\hat{A}_0 \equiv A_0 - \sum_r A_r \equiv A_{\rm mv} + A_s \tag{S20}$$

with the area $A_{\rm mv}$ of the redefined mother vesicle. If we envisage to inflate this mother vesicle to retract the selected tube without changing the remaining tubes, we obtain a spherical vesicle with radius $\hat{R}_0 = [\hat{A}_0/(4\pi)]^{1/2}$ and volume $\hat{V}_0 = \frac{4\pi}{3}\hat{R}_0^3$.

Now, we have to replace the quantities R_0, V_0, and A_0 in Eqs. S1 - S3 by $\hat{R}_0, \hat{V}_0$, and $\hat{A}_0$ and to repeat the whole calculation with the hatted variables. In this way, we study the growth of the selected tube while all the other tubes remain unchanged. As a result, we obtain the critical length $\hat{L}^*_{\rm tu} \approx 3\hat{R}_0$ for the selected tube. Because the redefined vesicle radius $\hat{R}_0$ is smaller than R_0, the critical length $\hat{L}^*_{\rm tu}$ is smaller than $L^*_{\rm tu}$ for a vesicle with a single tube. This difference can, however, be neglected for the VM-A and VM-B morphologies studied here. Indeed, after the first two deflation steps, the total area of all membrane tubes, $A = A_s + \sum_r A_r$, satisfies $A \leq 0.1A_0$, see Fig. 3a in the main text, which implies that $\hat{A}_0 > 0.9A_0$ and $\hat{R}_0 > 0.948R_0$

irrespective of which individual tube we select. Therefore, the critical tube length $\hat{L}^*_{\rm tu}$ of any selected tube lies within the interval $2.84\,R_0 < \hat{L}^*_{\rm tu} \leq 3R_0$ and is always much larger than the individual tube lengths observed for the VM-A and VM-B morphologies.

When a necklace-like tube with length $L^*_{\rm tu}$ is transformed into a cylindrical tube of equal area $A^*_{\rm tu}$, the tube length becomes twice as large. Therefore, in equilibrium, necklace-like tubes should have a length up to $L^*_{\rm tu}$ whereas cylindrical tubes should have a length exceeding $2L^*_{\rm tu}$. As a consequence, the length distribution of the tubes is predicted to exhibit a gap defined by the interval $L^*_{\rm tu} < L_{\rm tu} < 2L^*_{\rm tu}$.

S2 Critical tube length for VM-C morphologies

For the VM-C morphologies, the vesicle membrane is partially wetted by the two aqueous phases and the pe membrane segment separating the PEG-rich from the external phase forms the intrinsic contact angle $\theta_{\rm in}$ with the pd interface. For the lipid-polymer systems studied here, all intrinsic contact angles were smaller than 90° (Fig. 8c in the main text).

Because of partial wetting, a membrane tube can lower its free energy by adhering to the pd interface. Furthermore, the large separation of length scales between the weakly curved pd interfaces and the strongly curved membrane tubes implies that we can ignore the interfacial curvature and consider the adhesion of the tubes to planar interfaces. In order to obtain explicit expressions for the corresponding adhesion free energies, we also ignore possible deformations of the tube shapes by the adhesion.

S2.1 Adhesion free energy of necklace-like tube

First, consider a necklace-like tube consisting of N spherical beads with radius $R_{\rm ss} = 1/|m|$ as in Fig. S4a. A single bead will immerse into the dextran-rich phase until the angle between the pd interface and the pe segment of the bead membrane is equal to the intrinsic contact angle $\theta_{\rm in}$. In the following, we will first consider an arbitrary contact angle θ and then require that the adhesion free energy attains its lowest value when this contact angle is equal to the intrinsic contact angle $\theta_{\rm in}$.

When the tube membrane forms the contact angle θ with the pd interface, the total surface area $A_{\rm nl}$ of the necklace-like tube is partitioned into two segments according to

$$A_{\rm nl} = N\,4\pi R_{\rm ss}^2 = N4\pi|m|^{-2} = A_{\rm mp} + A_{\rm md} \tag{S21}$$

with the contact area

$$A_{\rm mp} = N\,2\pi R_{\rm ss}^2(1+\cos\theta) = N\,2\pi|m|^{-2}(1+\cos\theta) \tag{S22}$$

between the inner leaflet of the membrane and the PEG-rich phase and and the contact area

$$A_{\rm md} = N\,2\pi R_{\rm ss}^2(1-\cos\theta) = N\,2\pi|m|^{-2}(1-\cos\theta) \tag{S23}$$

between the inner leaflet of the membrane and the dextran-rich phase. At the same time, the area $A_{\rm pd}$ of the pd interface is reduced by

$$\Delta A_{\rm pd} = N\,\pi(R_{\rm ss}\sin\theta)^2 = N\,\pi|m|^{-2}\sin^2\theta \tag{S24}$$

The interfacial free energy of the pd interface and the free, non-adhering necklace fully immersed in the PEG-rich phase has the form

$$\mathcal{F}_{\rm nl,fr} = \Sigma_{\rm pd}\,A_{\rm pd} + \Sigma_{\rm mp}\,A_{\rm nl} \tag{S25}$$

with the interfacial tension $\Sigma_{\rm mp}$ of the interface between the inner leaflet of the membrane and the PEG-rich phase. Likewise, the interfacial free energy of the necklace adhering to the pd interface is given by

$$\mathcal{F}_{\rm nl,ad} = \Sigma_{\rm pd}\,(A_{\rm pd}-\Delta A_{\rm pd}) + \Sigma_{\rm mp}\,(A_{\rm nl}-A_{\rm md}) + \Sigma_{\rm md}\,A_{\rm md} \tag{S26}$$

with the interfacial tension $\Sigma_{\rm md}$ between the inner leaflet of the membrane and the dextran-rich phase. The adhesion free energy of the necklace-like tube is then given by

$$\mathcal{F}_{\rm nl} \equiv \mathcal{F}_{\rm nl,ad} - \mathcal{F}_{\rm nl,fr} = (\Sigma_{\rm md}-\Sigma_{\rm mp})\,A_{\rm md} - \Sigma_{\rm pd}\,\Delta A_{\rm pd} \tag{S27}$$

or

$$\mathcal{F}_{\rm nl} = A_{\rm nl}\left[\tfrac{1}{2}\,(\Sigma_{\rm md}-\Sigma_{\rm mp})(1-\cos\theta)\;-\tfrac{1}{4}\,\Sigma_{\rm pd}\sin^2\theta\right]\,. \tag{S28}$$

We now require that this free energy attains its equilibrium value when the contact angle θ becomes equal to the intrinsic contact angle $\theta_{\rm in}$ corresponding to $\partial\mathcal{F}_{\rm nl}/\partial\theta = 0$ for $\theta = \theta_{\rm in}$. This requirement leads to

$$\Sigma_{\rm md} - \Sigma_{\rm mp} = \Sigma_{\rm pd}\,\cos\theta_{\rm in} \tag{S29}$$

and to the equilibrium value

$$\mathcal{F}_{\rm nl}^{\rm eq} = A_{\rm nl}\,\Sigma_{\rm pd}\,g_{\rm nl}(\theta_{\rm in}) \tag{S30}$$

for the adhesion free energy of the necklace-like tube with the angle-dependent function

$$g_{\rm nl}(\theta) \equiv \tfrac{1}{2}\,\cos\theta(1-\cos\theta) - \tfrac{1}{4}\,\sin^2\theta = -\tfrac{1}{4}\,(1-\cos\theta)^2\,. \tag{S31}$$

The second expression for $g_{\rm nl}(\theta)$ implies that the adhesion free energy $\mathcal{F}_{\rm nl}^{\rm eq}$ is negative for nonzero values of the intrinsic contact angle $\theta_{\rm in}$, which shows explicitly that the adhering tube is energetically favored compared to the free tube immersed in the PEG-rich phase. Furthermore, the adhesion free energy density $\mathcal{F}_{\rm nl}^{\rm eq}/A_{\rm nl}$ as obtained from (S30) depends only on two material parameters, the interfacial tension $\Sigma_{\rm pd}$ of the pd interface and the intrinsic contact angle $\theta_{\rm in}$, both of which can be determined experimentally, see Fig. 3b and Fig. 8c in the main text.

S2.2 Adhesion free energy of cylindrical tube

Next, consider a cylindrical tube with two spherical end caps as in Fig. S4b. The body of the cylinder has length $L_{\rm cy}$ and radius $R_{\rm cy} = 1/(2|m|)$; the spherical end caps have the same radius as the cylinder. These two membrane segments have the areas

$$A_{\rm cy}^{\rm bod} = 2\pi R_{\rm cy} L_{\rm cy} = \frac{\pi}{|m|} L_{\rm cy} \quad \text{and} \quad A_{\rm cy}^{\rm cap} = 4\pi R_{\rm cy}^2 = \frac{\pi}{m^2}\,. \tag{S32}$$

When the tube membrane forms the contact angle θ with the pd interface, the tube area $A_{\rm cy}$ is partitioned according to

$$A_{\rm cy} = A_{\rm cy}^{\rm bod} + A_{\rm cy}^{\rm cap} = A_{\rm mp} + A_{\rm md} \tag{S33}$$

with the contact areas

$$A_{\rm mp} = 2(\pi - \theta) R_{\rm cy} L_{\rm cy} + 2\pi R_{\rm cy}^2 (1 + \cos\theta) \tag{S34}$$

and

$$A_{\rm md} = 2\theta R_{\rm cy} L_{\rm cy} + 2\pi R_{\rm cy}^2 (1 - \cos\theta)\,. \tag{S35}$$

At the same time, the area $A_{\rm pd}$ of the pd interface is reduced by

$$\Delta A_{\rm pd} = 2R_{\rm cy} L_{\rm cy} \sin\theta + \pi R_{\rm cy}^2 \sin^2\theta\,. \tag{S36}$$

The interfacial free energies $\mathcal{F}_{\rm cy,fr}$ and $\mathcal{F}_{\rm cy,ad}$ have the same general form as in (S25) and (S26). It then follows that the adhesion free energy of the cylindrical tube is given by

$$\mathcal{F}_{\rm cy} = A_{\rm cy}^{\rm bod}\, G_{\rm cy}^{\rm bod} + A_{\rm cy}^{\rm cap}\, G_{\rm cy}^{\rm cap} \tag{S37}$$

with the body contribution

$$G_{\rm cy}^{\rm bod} \equiv (\Sigma_{\rm md} - \Sigma_{\rm mp}) \frac{\theta}{\pi} - \Sigma_{\rm pd} \frac{\sin\theta}{\pi} \tag{S38}$$

and the cap contribution

$$G_{\rm cy}^{\rm cap} \equiv (\Sigma_{\rm md} - \Sigma_{\rm mp}) \tfrac{1}{2} (1 - \cos\theta) - \Sigma_{\rm pd} \tfrac{1}{4} \sin^2\theta\,. \tag{S39}$$

The equilibrium value of the contact angle θ is again imposed by the condition $\partial F_{\rm cy}/\partial\theta = 0$ for $\theta = \theta_{\rm in}$ which leads to the same relation $\Sigma_{\rm md} - \Sigma_{\rm mp} = \Sigma_{\rm pd} \cos\theta_{\rm in}$ as in (S29). As a consequence, the adhesion free energy of the capped cylindrical tube has the equilibrium form

$$\mathcal{F}_{\rm cy}^{\rm eq} = \Sigma_{\rm pd} A_{\rm cy}^{\rm bod}\, g_{\rm cy}(\theta_{\rm in}) + \Sigma_{\rm pd}\, A_{\rm cy}^{\rm cap}\, g_{\rm nl}(\theta_{\rm in}) \tag{S40}$$

with the function

$$g_{\rm cy}(\theta) \equiv \frac{\theta}{\pi} \cos\theta - \frac{\sin\theta}{\pi} \tag{S41}$$

and the function $g_{\rm nl}(\theta)$ as defined in (S31).

S2.3 Critical area and critical length of adhering tubes

We now compare an adhering necklace-like tube with an adhering cylindrical tube of the same tube area $A_{\rm tu}$ which then satisfies

$$A_{\rm tu} = A_{\rm cy} = A_{\rm nl}\,. \tag{S42}$$

The bending energy of the necklace-like tube vanishes whereas the capped cylinder has the bending energy $2\pi\kappa$ arising from the spherical end caps as in (S12). Therefore, we have to consider the free energy difference

$$\Delta\mathcal{F} = \mathcal{F}_{\rm cy}^{\rm eq} + 2\pi\kappa - \mathcal{F}_{\rm nl}^{\rm eq} \tag{S43}$$

which can be rewritten in the form

$$\Delta\mathcal{F} = 2\pi\kappa - \Sigma_{\rm pd} A_{\rm tu} \left[1 - \frac{\pi}{m^2 A_{\rm tu}}\right] g(\theta_{\rm in}) \tag{S44}$$

with the function

$$g(\theta) \equiv g_{\rm nl}(\theta) - g_{\rm cy}(\theta) = \tfrac{1}{\pi}\left(\sin\theta - \theta\cos\theta\right) - \tfrac{1}{4}\left(1-\cos\theta\right)^2. \tag{S45}$$

As shown in Fig. S4c, the function $g(\theta)$ is positive for $0 < \theta < \pi$. Therefore, the shape of the adhering tube is determined by the competition between the bending energy $2\pi\kappa$ of the spherical caps, which favors necklace-like tubes, and the adhesion free energy, which favors cylindrical tubes. The spherical cap energy is independent of the tube area whereas the adhesion free energy is proportional to this area. As a consequence, short adhering tubes are necklace-like whereas long adhering tubes are cylindrical. These two regimes are separated by the critical tube area

$$A_{\rm tu}^* = \frac{2\pi\kappa}{\Sigma_{\rm pd}\, g(\theta_{\rm in})} + \frac{\pi}{m^2} \tag{S46}$$

as follows from $\Delta\mathcal{F} = 0$. The first term directly reflects the interplay between the membrane's bending rigidity κ, the interfacial tension $\Sigma_{\rm pd}$, and the intrinsic contact angle $\theta_{\rm in}$ for partial wetting. The second term on the right hand side of (S46) represents a correction term arising from the spherical end caps.

In Fig. S4d, we compare the free energies of single necklace-like and cylindrical tubes as a function of tube area $A_{\rm tu}$ for the Ld_4 and the Lo_4 vesicles. The critical tube area is about $4.4\,\mu{\rm m}^2$ for the Ld_4 vesicle and about $80.7\,\mu{\rm m}^2$ for the Lo_4 vesicle.

From an experimental point, it is easier to measure the length of individual tubes rather than their area. The critical length $L_{\rm ad}^* = N_{\rm ad}^* 2/|m|$ of the necklace-like tube with the critical bead number $N_{\rm ad}^*$ is given by

$$L_{\rm ad}^* = A_{\rm tu}^* \frac{|m|}{2\pi} = \frac{\kappa|m|}{\Sigma_{\rm pd}\, g(\theta_{\rm in})} + \frac{1}{2|m|}\,. \tag{S47}$$

When a necklace-like tube with length $L_{\rm ad}^*$ is transformed into a cylindrical tube of equal area $A_{\rm tu}^*$, the tube length becomes twice as large. Therefore, in equilibrium,

necklace-like tubes should have a length up to $L^*_{\rm ad}$ whereas cylindrical tubes should have a length exceeding $2L^*_{\rm ad}$. For the example displayed in Fig. S4d corresponding to the fourth deflation step, the critical tube length $L^*_{\rm ad}$ is 5.6 μm for the Ld_4 vesicle and 21.4 μm for the Lo_4 vesicle.

S3 Tube flexibility and persistence length

The flexibility of membrane nanotubes can be characterized by the persistence length for tube bending. This length scale governs the exponential decay of the two-point correlation function between unit tangent vectors along the tube, in close analogy to semiflexible polymers [4, 5]. A cylindrical tube of radius $R_{\rm cy}$ has the persistence length [6, 7]

$$\xi_p = 2\pi\kappa R_{\rm cy}/(k_{\rm B}T)\,. \tag{S48}$$

For $R_{\rm cy} = 1/(2|m|)$ corresponding to the state of lowest bending energy, this expression becomes

$$\xi_p = \frac{\pi\kappa}{|m|k_{\rm B}T}\,. \tag{S49}$$

Using the overall partitioning of the membrane area with total tube area A and total tube length L, a cylindrical tube has the spontaneous curvature $|m| = \pi L/A$ which implies the persistence length

$$\xi_p = \frac{\kappa}{k_{\rm B}T}\frac{A}{L} \quad \text{(cylindrical tube)}\,. \tag{S50}$$

The persistence length of the necklace-like tube, on the other hand, is comparable to the diameter $2R_{\rm ss} = 2/|m|$ of the small spheres which implies

$$\xi_p \simeq 2R_{\rm ss} = \frac{1}{\pi}\frac{A}{L} \quad \text{(necklace-like tube)}\,. \tag{S51}$$

For the Ld membrane studied here, the bending rigidity $\kappa_{\rm Ld} = 0.82 \times 10^{-19}\,$J and $\kappa_{\rm Ld}/(k_{\rm B}T) = 20$ at room temperature (25°C). For the Ld_1 vesicle, we obtained the total tube area $A = 473\,\mu{\rm m}^2$ and the total tube length $L = 600\,\mu$m. If the tubes were cylindrical, we would obtain the spontaneous curvature $|m| = 1/(0.251\,\mu{\rm m})$ and the persistence length $\xi_p = 15.4\,\mu$m. If the tubes were necklace-like, we would obtain the spontaneous curvature $|m| = 1/(0.125\,\mu{\rm m})$ and the persistence length $\xi_p \simeq 0.25\,\mu$m. Inspection of the Movies Ld_1 and Ld_2 reveals that the thermal fluctuations of the tubes lead to hairpin-like conformations with curvature radii of the order of $2\,\mu$m which implies a persistence length below $2\,\mu$m. Such an upper bound for the persistence length is consistent with a necklace-like but not with a cylindrical tube morphology.

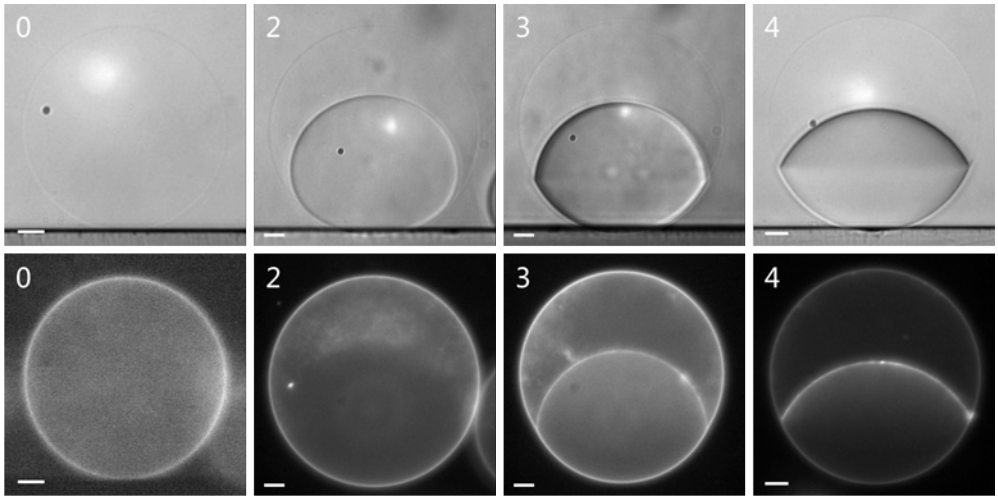

Figure S1: **Shapes of aqueous droplets for different vesicle morphologies:** The images correspond to Ld_j vesicles after the jth deflation step with $j = 0, 2, 3,$ and 4 as observed by differential interference contrast (DIC) microscopy (top row) and fluorescence microscopy (bottom row). The two images with the same j-value display the same vesicle. The white scale bar is 10 μm in all panels. The images were obtained by a horizontally aligned inverted microscope (Axiovert 135, Zeiss) equipped with a 40x long distance objective and a mono-color camera.

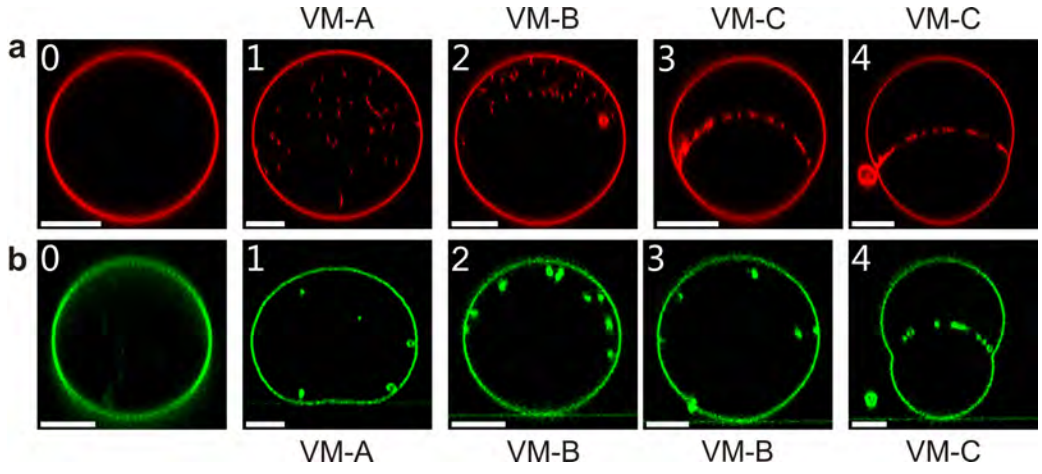

Figure S2: **Vertical cross sections of the Ld and Lo vesicles in Fig. 2: (a)** Confocal xz-scans of the Ld_j vesicles in Fig. 2c; and **(b)** Confocal xz-scans of the Lo_j vesicles in Fig. 2d. The three vesicle morphologies VM-A, VM-B, and VM-C are explained in Fig. 1.

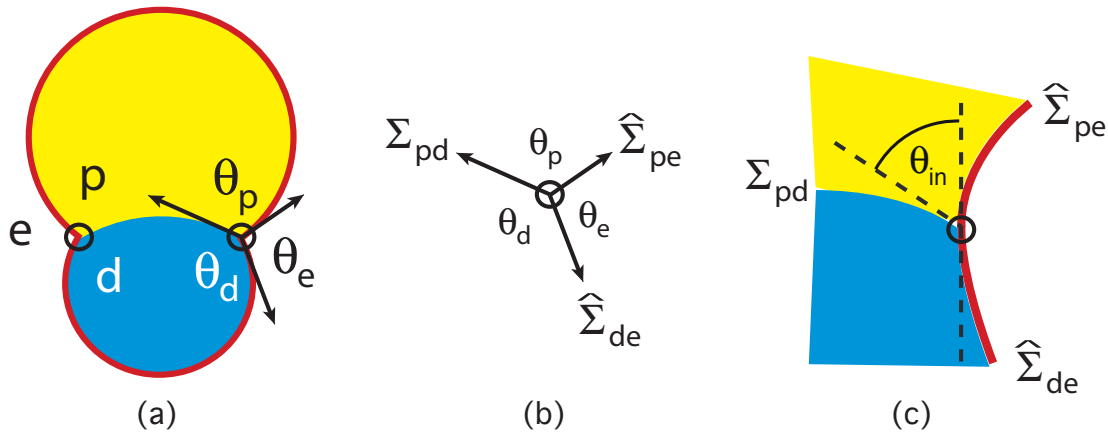

Figure S3: **Contact angles for the VM-C morphology:** The latter morphology involves one droplet of the PEG-rich phase p (yellow) and one droplet of the dextran-rich phase d (blue), both embedded in the exterior phase e (white): **(a)** The pd interface meets the membrane (red) along the contact line (two black circles). The latter line divides the membrane up into two segments, the pe segment between the PEG-rich droplet and the exterior phase as well as the de segment between the dextran-rich droplet and the exterior phase. When viewed with optical resolution, the membrane exhibits a kink at the contact line which defines the effective contact angles $\theta_{\rm p}, \theta_{\rm d}$, and $\theta_{\rm e}$; **(b)** The three arrows represent the interfacial tension $\Sigma_{\rm pd}$ as well as the two membrane tensions $\hat{\Sigma}_{\rm pe}$ and $\hat{\Sigma}_{\rm de}$ within the pe and de segments of the membrane. Mechanical equilibrium implies that the three tension vectors add up to zero; and **(c)** Enlarged view of the smoothly curved membrane (red) close to the contact line (black circle). The vertical broken line represents the common tangent plane of the two membrane segments. The angle between this common tangent plane and the plane tangential to the pd interface provides the intrinsic contact angle $\theta_{\rm in}$. [8] The membrane nanotubes have been omitted here in order to focus on the shape of the mother vesicle.

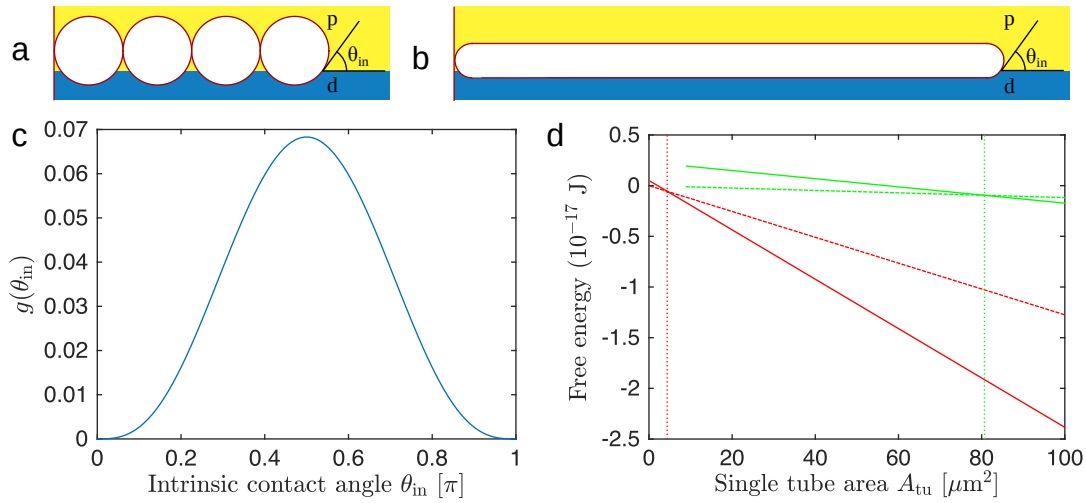

Figure S4: **Adhesion of membrane nanotubes to the pd interface (VM-C morphology): (a)** Necklace-like tube with four spherical beads and **(b)** Cylindrical tube with the same membrane area. Both tubes adhere to the pd interface which separates the PEG-rich phase p (yellow) from the dextran-rich phase d (blue) and forms the intrinsic contact angle θ_{in} with the tube membranes; **(c)** Functional dependence of the dimensionless free energy difference g on the intrinsic contact angle θ_{in} as given by equation (S45); and **(d)** Free energies of single necklace-like (dashed) and cylindrical (solid) tube protruding into the Ld_4 (red) and Lo_4 (green) vesicle as a function of tube area A_{tu} with $A_{\text{tu}} \geq 8\pi/m^2$ where the latter area corresponds to the 2-bead necklace $L^{[2]}$. The dashed and solid lines cross at the critical tube area A^*_{tu} which is equal to $4.4\,\mu\text{m}^2$ for the Ld_4 vesicle and to $80.7\,\mu\text{m}^2$ for the Lo_4 vesicle. The corresponding critical tube lengths are given by $L^*_{\text{tu}} = 5.6\,\mu\text{m}$ for the Ld_4 and by $L^*_{\text{tu}} = 21.4\,\mu\text{m}$ for the Lo_4 vesicle. The free energy of the necklace-like tubes is given by $\mathcal{F}^{\text{eq}}_{\text{nl}}$ as in equation (S30); the free energy of the cylindrical tubes is equal to $\mathcal{F}^{\text{eq}}_{\text{cy}} + 2\pi\kappa$ with $\mathcal{F}^{\text{eq}}_{\text{cy}}$ as in equation (S40).

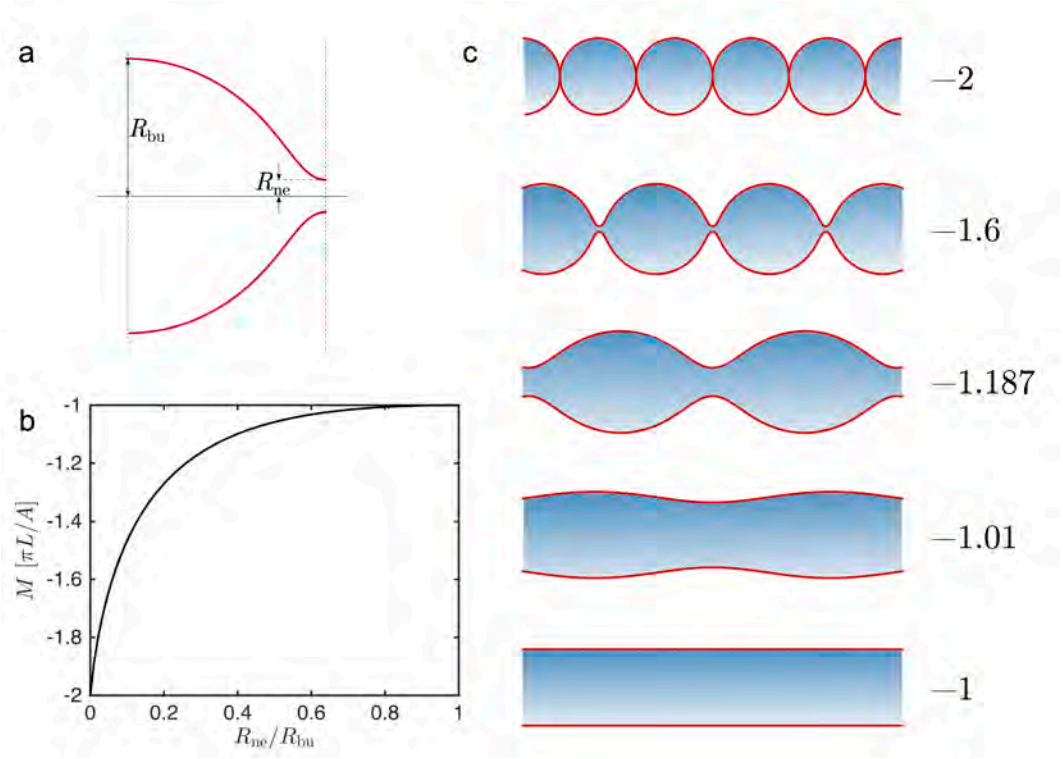

Figure S5: **Different tube shapes with the same membrane area and tube length: (a)** Each unit cell of an unduloid is characterized by its neck radius $R_{\rm ne}$ and its bulge radius $R_{\rm bu}$. The necklace-like tube corresponds to the ratio $R_{\rm ne}/R_{\rm bu} = 0$, the cylindrical tube to $R_{\rm ne}/R_{\rm bu} = 1$; **(b)** For given membrane area A and tube length L, the mean curvature M increases monotonically from $M = -2\pi L/A$ for the necklace-like tube to $M = -\pi L/A$ for the cylindrical tube; and **(c)** Three examples of unduloids for fixed A and L that interpolate between the necklace-like and the cylindrical tube with mean curvature M in units of $\pi L/A$ (right column). As we transform the sphere-necklace into the cylinder, the neck radius $R_{\rm ne}$ of the intermediate unduloid increases monotonically whereas the bulge radius $R_{\rm bu}$ first increases and then decreases again. The latter radius has the value $A/(2\pi L)$ both for the cylindrical tube and for the sphere-necklace and attains its maximum at $M = m = -1.187\pi L/A$ with $\max(R_{\rm bu}) = 0.662A/\pi L$.

Table S1: **Deflation path within the phase diagram of Fig. 2:** The deflation path in Fig. 2a,b consists of seven deflation steps which lead to seven compositions of the aqueous polymer solution within the vesicle, labeled from $j = 1$ to $j = 7$. The initial compositions in the exterior and interior solution are denoted by 0e and 0. The columns 2 - 7 display the following quantities: Dextran weight fraction $w_{\rm d}$, PEG weight fraction $w_{\rm p}$, total polymer mass density c_j of the interior solution, as well as concentration ratio c_j/c_0, osmolarity ratio $P_{\rm e}/P_0$ between the exterior and the initial osmolarities, $P_{\rm e}$ and P_0. The exterior osmolarity $P_{\rm e}$ is increased by exchanging the external medium by a hypertonic solution with constant $w_{\rm d} = w_{\rm p} = 0.0327$ and an increasing weight fraction of sucrose. For $j \geq 0$, the weight fractions $w_{\rm d}$ and $w_{\rm p}$ represent the weight fractions of all dextran and all PEG molecules within the interior solution, irrespective of whether this solution is uniform or phase separated, and are characterized by the constant ratio $w_{\rm d}/w_{\rm p} = 1.25$. For comparison, the quantities at the critical point (cr) are also included. 'APS' stands for 'aqueous phase separation' in the vesicle interior. The last two rows describe the observed vesicle morphologies of the liquid-disordered (Ld) and liquid-ordered (Lo) membranes. The VM-B and VM-C morphologies correspond to phase separation with complete and partial wetting, respectively, of the membranes by the PEG-rich phase.

comp. j	$w_{\rm d}$	$w_{\rm p}$	c_j [g/cm^3]	c_j/c_0	$P_{\rm e}/P_0$	APS	Ld morph.	Lo morph.
0e	0.0327	0.0327	0.0664		1.000	no		
0	0.0390	0.0312	0.0714	1.000	1.000	no		
1	0.0436	0.0349	0.0800	1.120	1.254	no	VM-A	VM-A
cr	0.0451	0.0361	0.0829	1.161	1.350	no		
2	0.0456	0.0365	0.0838	1.174	1.382	yes	VM-B	VM-B
3	0.0475	0.0380	0.0875	1.224	1.511	yes	VM-C	VM-B
4	0.0494	0.0395	0.0909	1.273	1.642	yes	VM-C	VM-C
5	0.0511	0.0408	0.0941	1.317	1.769	yes	VM-C	VM-C
6	0.0527	0.0422	0.0972	1.361	1.901	yes	VM-C	VM-C
7	0.0543	0.0434	0.1002	1.402	2.032	yes	VM-C	VM-C

Table S2: **Geometry of deflated Ld_j and Lo_j vesicles:** The first four rows give the lipid phase, the deflation step number (or polymer composition) j corresponding to the Table S1, the vesicle morphology, and the osmolarity ratio P_e/P_0. The following rows contain the initial vesicle volume V_0, the initial area A_0, and the initial radius R_0 before the first deflation step, the apparent volume V_{app} and the apparent area A_{app} of the mother vesicle after the deflation step j, the total tube area $A = A_0 - A_{app}$, the total tube length L, and the fraction Λ of the total tube length corresponding to cylindrical tubes.

vesicle	Ld_1	Ld_2	Ld_3	Ld_4	Lo_1	Lo_2	Lo_3	Lo_4
lipid phase	Ld	Ld	Ld	Ld	Lo	Lo	Lo	Lo
defl. step j	1	2	3	4	1	2	3	4
morph.	VM-A	VM-B	VM-C	VM-C	VM-A	VM-B	VM-B	VM-C
P_e/P_0	1.25	1.38	1.51	1.64	1.25	1.38	1.51	1.64
V_0 [μm^3]	49296	30138	10223	30590	37384	14991	35177	37210
A_0 [μm^2]	6500	4683	2278	4730	5407	2940	5192	5390
R_0 [μm]	22.7	19.3	13.5	19.4	20.7	15.3	20.3	20.7
V_{app} [μm^3]	43997	25671	8350	24030	33378	12770	28730	29230
A_{app} [μm^2]	6027	4208	1992	4049	5053	2642	4536	4754
A [μm^2]	473	475	286	681	354	298	656	636
L [μm]	600	600	395	953	94	100	200	195
Λ	0	0	$\frac{1}{2} \pm \frac{1}{2}$ [a]	$\frac{1}{2} \pm \frac{1}{2}$ [a]	0	0	0	0.46

[a] For the VM-C morphology of the Ld membranes, we used the estimate $\Lambda = \frac{1}{2} \pm \frac{1}{2}$ corresponding to the whole range $0 \leq \Lambda \leq 1$ of possible Λ-values.

Table S3: **Overlap of PEG and dextran chains along the deflation path:** The osmotic deflation steps generate the compositions j with total polymer concentration c_j inside the vesicles, irrespective of whether the interior solution is uniform or phase separated. This concentration determines the reduced polymer concentration $\epsilon = |c_{\rm cr} - c|/c_{\rm cr}$ which measures the distance from the critical consolute point with concentration $c_{\rm cr}$. For the PEG and dextran chains studied here, the radii of gyration have been estimated to be $R_{\rm p} = 4.05\,{\rm nm}$ and $R_{\rm d} = 21\,{\rm nm}$. [9] The overlap concentrations of PEG and dextran are then given by $1/[(4\pi/3)R_{\rm p}^3] = 0.00359/{\rm nm}^3$ and $1/[(4\pi/3)R_{\rm d}^3] = 0.0258/(10\,{\rm nm})^3$ which are equivalent to the overlap weight fractions $w_{\rm p}^* = 0.0477$ and $w_{\rm d}^* = 0.0193$. We characterize the degree of overlapping and the associated strength of repulsive chain-chain interactions by the overlap ratios $w_{\rm p}/w_{\rm p}^*$ and $w_{\rm d}/w_{\rm d}^*$. Columns 4 and 5 display the overlap ratios of the PEG and dextran chains within the one-phase region. In this region, the large dextran chains overlapped already at the lowest dextran concentration while the smaller PEG chains did not overlap with each other but always overlapped with the dextran chains. The corresponding ratios after phase separation are shown in columns 6 and 7 for the PEG-rich phase as well as in columns 8 and 9 for the dextran-rich phase. In the PEG-rich phase, the overlap of the PEG chains increased with each deflation step whereas the dextran chains became separated after the third step. In the dextran-rich phase, the dextran chains overlapped more and more strongly whereas the PEG chains became more and more dilute but had to overlap with the dextran chains. Thus, all polymer solutions along the deflation path were semi-dilute.

comp. j	c_j [g/cm^3]	ϵ	$\frac{w_{\rm p}}{w_{\rm p}^*}$	$\frac{w_{\rm d}}{w_{\rm d}^*}$	$\frac{w_{\rm p}^{\rm PE}}{w_{\rm p}^*}$	$\frac{w_{\rm d}^{\rm PE}}{w_{\rm d}^*}$	$\frac{w_{\rm p}^{\rm DE}}{w_{\rm p}^*}$	$\frac{w_{\rm d}^{\rm DE}}{w_{\rm d}^*}$
0e	0.0664		0.69	1.69				
0	0.0714	0.139	0.65	2.02				
1	0.0800	0.035	0.73	2.26				
cr	0.0829	0	0.76	2.34				
2	0.0838	0.011			0.94	1.36	0.57	3.53
3	0.0875	0.055			1.09	0.79	0.46	4.42
4	0.0909	0.097			1.18	0.56	0.39	5.03
7	0.1002	0.209			1.38	0.25	0.28	6.78

Movie Ld_1: Morphology VM-A of Ld membrane

Giant vesicle bounded by an Ld membrane (red) after the first deflation step. The interior aqueous solution had total polymer mass density $c_1 = 1.120\, c_0 = 0.965\, c_{\rm cr}$ and formed a uniform aqueous phase within the giant vesicle. The movie contains the 3-dimensional scan of the vesicle, provided by a stack of 44 confocal scans corresponding to different separations z from the cover slide, varying from $z = 1\,\mu$m to $z = 44\,\mu$m in increments of $1\,\mu$m. The scan reveals many nanotubes that protrude into the vesicle interior. The thickness of these tubes is below optical resolution; the total tube length is $600 \pm 100\,\mu$m.

Movie Ld_2: Morphology VM-B of Ld membrane

Giant vesicle with an Ld membrane (red) after the second deflation step. The interior aqueous solution had total polymer mass density $c_2 = 1.174\, c_0 = 1.024\, c_{\rm cr}$ and was separated into two aqueous phases forming a PEG-rich and a dextran-rich droplet. The membrane was completely wetted by the PEG-rich phase and, thus, not in contact with the pd interface between the two aqueous droplets. The movie contains the 3-dimensional scan of the vesicle, provided by a stack of 37 confocal scans corresponding to different separations z from the cover slide, varying from $z = 1\,\mu$m to $z = 37\,\mu$m in increments of $1\,\mu$m. The Ld membrane has formed many nanotubes that protrude into the vesicle interior but are excluded from the dextran-rich phase which is in touch with the cover slide and thus located at low z-values. The thickness of these tubes is below optical resolution; the total tube length is $600 \pm 100\,\mu$m.

Movie Ld_4: Morphology VM-C of Ld membrane

Giant vesicle with an Ld membrane (red) after the fourth deflation step. The interior aqueous solution had total polymer mass density $c_4 = 1.273\, c_0 = 1.097\, c_{\rm cr}$ and was phase separated into a PEG-rich and a dextran-rich droplet. The membrane was partially wetted by the PEG-rich phase and formed effective contact angles, $\theta_{\rm p}$ and $\theta_{\rm d}$, with the pd interface between the two aqueous droplets (Fig. S3a). The movie contains the 3-dimensional scan of the vesicle, provided by a stack of 82 confocal scans corresponding to different separations z from the cover slide, varying from $z = 0.5\,\mu$m to $z = 41\,\mu$m in increments of $0.5\,\mu$m. The scan shows many nanotubes that protrude into the vesicle interior and aggregate at the pd interface because of partial wetting. The thickness of these tubes is below optical resolution; the total tube length is $953 \pm 150\,\mu$m.

Movie Lo_1: Morphology VM-A of Lo membrane

Giant vesicle with an Lo membrane (green) after the first deflation step. The interior aqueous solution had total polymer mass density $c_1 = 1.120\, c_0 = 0.965\, c_{\rm cr}$ and formed a uniform aqueous phase within the vesicle. The movie contains the 3-dimensional scan of the vesicle, provided by a stack of 74 confocal scans corresponding to different separations z from the cover slide, varying from $z = 0.5\,\mu$m to $z = 37\,\mu$m in increments of $0.5\,\mu$m. The Lo membrane has formed many nanotubes that protrude into the vesicle interior. The tube morphology can be optically resolved and is provided by short necklace-like tubes; the total tube length is $94 \pm 14\,\mu$m.

Movie Lo_2: Morphology VM-B for Lo membrane

Giant vesicle with an Lo membrane (green) after the second deflation step. The interior aqueous solution had total polymer mass density $c_2 = 1.174\, c_0 = 1.024\, c_{\rm cr}$ and was phase separated into a PEG-rich and a dextran-rich droplet. The membrane was completely wetted by the PEG-rich phase and, thus, not in contact with the pd interface between the two aqueous droplets. The movie contains the 3-dimensional scan of the vesicle, provided by a stack of 58 confocal scans corresponding to different separations z from the cover slide, varying from $z = 0.5\,\mu$m to $z = 29\,\mu$m in increments of $0.5\,\mu$m. The scan reveals many nanotubes protruding into the vesicle interior without entering the dextran-rich phase which is in touch with the cover slide and thus located at low z-values. The tube morphology can be optically resolved and is provided by necklace-like tubes with an average bead radius of $0.63 \pm 0.10\,\mu$m.

Movie Lo_4: Morphology VM-C for Lo membrane

Giant vesicle with an Lo membrane (green) after the fourth deflation step. The interior aqueous solution had total polymer mass density $c_4 = 1.273\, c_0 = 1.097\, c_{\rm cr}$ and was phase separated into a PEG-rich and a dextran-rich droplet. The membrane was partially wetted by the PEG-rich phase and formed effective contact angles, $\theta_{\rm p}$ and $\theta_{\rm d}$, with the pd interface between the two aqueous droplets (Fig. S3a). The movie contains the 3-dimensional scan of the vesicle, provided by a stack of 74 confocal scans corresponding to different separations z from the cover slide, varying from $z = 0.5\,\mu$m to $z = 37\,\mu$m in increments of $0.5\,\mu$m. The Lo membrane has formed long nanotubes that protrude into the vesicle interior and tend to aggregate at the pd interface because of partial wetting. Detailed analysis of this scan (Fig. 6 in the main text) reveals the coexistence of necklace-like tubes with bead radius $R_{\rm ss} = 0.64 \pm 0.12\,\mu$m and cylindrical tubes with tube diameter $2R_{\rm cy} = 0.55 \pm 0.07\,\mu$m.

References

[1] Seifert, U., Berndl, K. & Lipowsky, R. Shape Transformations of Vesicles: Phase Diagram for Spontaneous Curvature and Bilayer Coupling Model. *Phys. Rev. A* **44**, 1182–1202 (1991).

[2] Lipowsky, R. Coupling of Bending and Stretching Deformations in Vesicle Membranes. *Adv. Colloid Interface Sci.* **208**, 14–24 (2014).

[3] Lipowsky, R. Spontaneous Tubulation of Membranes and Vesicles Reveals Membrane Tension Generated by Spontaneous Curvature. *Faraday Discuss.* **161**, 305–331 (2013).

[4] Doi, M. & Edwards, S. *The Theory of Polymer Dynamics* (Clarendon Press, Oxford, 1986).

[5] Kierfeld, J., Niamploy, O., Sa-yakanit, V. & Lipowsky, R. Stretching of Semiflexible Polymers with Elastic Bonds. *Eur. Phys. J. E* **14**, 17–34 (2004).

[6] Helfrich, W. & Harbich, W. Adhesion and Cohesion of Tubular Vesicles. *Chemica Scripta* **25**, 32–36 (1985).

[7] Baroji, Y. F., Oddershede, L. B., Reihani, S. N. S. & Bendix, P. M. Fluorescent Quantification of Size and Lamellarity of Membrane Nanotubes. *Eur. Biophys. J.* **43**, 595–602 (2014).

[8] Kusumaatmaja, H., Li, Y., Dimova, R. & Lipowsky, R. Intrinsic Contact Angle of Aqueous Phases at Membranes and Vesicles. *Phys. Rev. Lett.* **103**, 238103 (2009).

[9] Liu, Y., Lipowsky, R. & Dimova, R. Concentration Dependence of the Interfacial Tension for Aqueous Two-Phase Polymer Solutions of Dextran and Polyethylene Glycol. *Langmuir* **28**, 3831–3839 (2012).